UCLA

Title

Solution-Processed Fabrication of One-Dimensional Photonic Crystals: Demonstrating Device Tunability and Perovskite Compatibility for Scalable, Efficient Optoelectronics

Permalink

Author

Katz, Daniel Joseph

Publication Date

2022

Peer reviewed|Thesis/dissertation

UNIVERSITY OF CALIFORNIA

Los Angeles

Solution-Processed Fabrication of One-Dimensional Photonic Crystals: Demonstrating Device

Tunability and Perovskite Compatibility for Scalable, Efficient Optoelectronics

A thesis submitted in partial satisfaction of the

requirements for the degree Master of Science

in Chemical Engineering

by

Daniel Joseph Katz

2022

ABSTRACT OF THE THESIS

Solution-Processed Fabrication of One-Dimensional Photonic Crystals: Demonstrating Device

Tunability and Perovskite Compatibility for Scalable, Efficient Optoelectronics

by

Daniel Joseph Katz

Master of Science in Chemical Engineering

University of California, Los Angeles, 2022

Professor Carissa N. Eisler, Chair

As global power consumption continues to rapidly increase the need for efficient, economically

feasible, and environmentally conscious energy sources has become clear. In accordance with

these sustainable efforts, the presented thesis details the development of an entirely

solution-processed Distributed Bragg Reflector (DBR) continuum which circumvents the energy

intensive processes usually needed to fabricate these optoelectronic environments. These

mirrors were created through alternative spincoating of titania sol gel and polymethyl

methacrylate (PMMA) films atop a glass substrate. A series of tests were conducted to derive a

model for the effective titania sol gel film refractive index as a function of wavelength, as this

quantity is highly dependent on experimental workup. Atomic force microscopy measurements

have confirmed that these individual layers are sufficiently thin (on the order of hundreds of

nanometers) and thus the resulting DBR structures have the desired thicknesses (on the order

of micrometers) for use in real device applications. The

reflectance spectra for these mirrors contain well-defined photonic bandgaps that span nearly 400 nm of the visible light wavelength regime, and retain peak heights on the order of 90%. These attributes make the reflectors suitable for use in lasing, LED, and next-generation solar device applications. Following the success of the DBR continuum, an entirely solution-processed luminescent solar concentrator design was formulated: green-emitting photoluminescent nanocrystals placed between two green-reflecting DBR mirrors. In-air, room temperature $CsPbBr_3$ perovskite syntheses produced nanocrystals with narrow emission bands in this regime that possessed all of the expected absorbance and photoluminescence spectra features. Preliminary work was done to stabilize these perovskites between two titania sol gel films - their effective local environment in the luminescent solar concentrator design that largely extinguishes any emission from these crystals. Power measurements taken inside an integrating sphere setup exemplified the preliminary success of using polystyrene to interface between the nanocrystals and surrounding titania films in this role. Future directions hope to improve upon this result, as well as continue to optimize the DBR mirror geometry. Following the eventual success of the green luminescent solar concentrator, attention will be given to other color domains in pursuit of the ultimate goal of this study: transforming the present DBR continuum into an entirely solution-processed luminescent solar concentrator continuum to be used as a basis for multijunction solar cell design.

The thesis of Daniel Joseph Katz is approved.

Panagiotis D. Christofides

Samanvaya Srivastava

Carissa N. Eisler, Committee Chair

University of California, Los Angeles

2022

Table of Contents

List of Figures and Tables

List of Acronyms

1.) 1D: One-dimensional

2.) DBR: Distributed Bragg Reflector

3.) AFM: Atomic Force Microscopy

4.) CNSI: California NanoSystems Institute

5.) DDAB: Didodecyldimethylammonium bromide

6.) FWHM: full at width half maximum

7.) LED: Light-emitting diode

8.) LSC: Luminescent Solar Concentrator

9.) NC: Nanocrystal

10.) NP: Nanoparticle

11.) OLED: Organic light-emitting diode

12.) PL: Photoluminesence

13.) PLNC: Photoluminescent nanocrystal

14.) PLQY: Photoluminescent quantum yield

15.) PMMA: Polymethyl methacrylate

16.) PS: Polystyrene

17.) RI: Refractive Index

18.) TOPO: Trioctylphosphine oxide

19.) TIR: Total internal reflection

20.) TMM: Transfer Matrix Method

21.) TTIP: Titanium isopropoxide

Chapter 1: Introduction

1.1 Motivation

Climate change is the greatest challenge global society will face within the existing population's lifetime. Greenhouse gas concentrations, sea level increase, and ocean acidification reached record high levels in 2021 [1]. These key climate change indicators suggest that planetary health is diminishing, and significant infrastructural changes must be made immediately. Copious amounts of evidence have documented the negative impact of traditional energy production practices on environmental wellbeing, and the United States Energy Information Administration predicts that world energy consumption will increase by 50% by the year 2050 [2]. Though this premise is daunting, sustainable energy is projected to be the fastest growing energy source between present day and the year 2050 [2]. The United Nations has repeatedly emphasized that deviation from fossil fuels and investment in renewable energy sources is paramount to saving the planet, and has outlined several pillars upon which this transition must be based in order to make this change feasible [1]. These pillars are touted as guiding principles for the presented study: solution-processed fabrication of one-dimensional photonic crystals for scalable, efficient optoelectronics.

These crystalline structures are key components of any devices that require waveguide components. This constitutes many categories of photonic-based technology including lasers, LEDs, and Luminescent Solar Concentrators (LSCs) - distinct chemical environments noted for their mechanical versatility, ability to efficiently concentrate incident light, and capacity to shape photonic spectra [3]. The presented design combines key components of contemporary solar research, photonic crystals and photoluminescent nanocrystals, to provide a solution-processed waveguide continuum while aligning with the aforementioned sustainability

principles of the United Nations. These photonic crystals aim to ease fabrication of the

aforementioned device components while driving up overall efficiency of these technologies.

The foremost overlap of these goals with those of the United Nations is seen in the call for

global access to renewable energy device components and raw materials – specifically

diversification of manufacturing and the capacity to do so at a global scale [1]. By deviating from

expensive, traditional photonic crystal fabrication methods and instead focusing on

solution-processed manufacturing, industrial-scale production becomes more financially feasible

and environmentally friendly. The improved device efficiency and use of accessible materials

will further this goal and simultaneously ease the transition from a fossil fuel infrastructure to a

renewable-based society.

1.2 Photonic Crystals

Photonic crystals are optical environments that are used in an array of optoelectronic devices

such as LED's, lasers, and new-generation photovoltaics [4]. They are defined as periodic

dielectric structures such as alternating layered stacks, periodic cylindrical arrays, and opals.

Similar to how a periodic array of atoms can create an electronic bandgap, this periodicity leads

to the formation of a photonic band gap: a regime of electromagnetic wavelengths at which

corresponding photons are either forbidden or encouraged to pass through the crystal in

question, creating a reflection of light [5]. The photonic bandgap is also commonly referred to as

the reflectance band or stop band. How reflective the photonic bandgap is, what wavelengths it

occurs at, and the bandwidth of wavelengths is determined by the periodicity and refractive

indices of the materials used. These structures can be single or multidimensional, and are

fabricated through a wide variety of processes. One-dimensional (1D) cavity-containing photonic

crystals have received the field's attention due to their ability to direct and concentrate photons

within their photonic bandgaps along the longitudinal axis of their structures [4]. The most

common, cavity-free 1D structures are composed of alternatively layered high and low refractive

index (RI) materials and are referred to as Distributed Bragg Reflectors (DBRs).
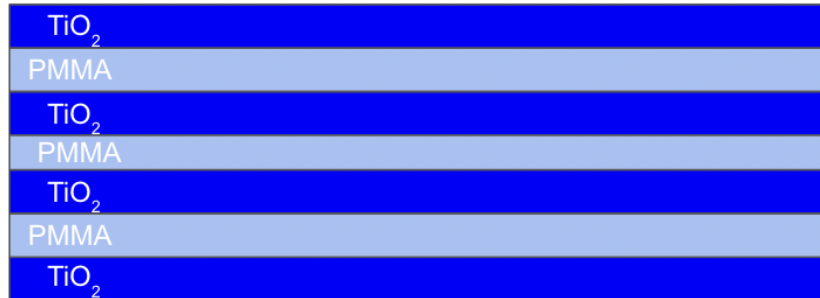
Figure 1: Exemplary TiO_2:PMMA Distributed Bragg Reflector. The periodic structure is composed of alternating low refractive index PMMA and high refractive index TiO_2 layers.

These DBR structures have tunable photonic bandgaps, whose wavelength locations are

dependent on device layer thickness, dielectric material, thermal treatment, and so on. DBRs

are often referred to as bragg mirrors, bragg stacks, and waveguides interchangeably. When

electromagnetic radiation is incident upon any medium it is either absorbed, transmitted, or

reflected as exemplified in Figure 2:
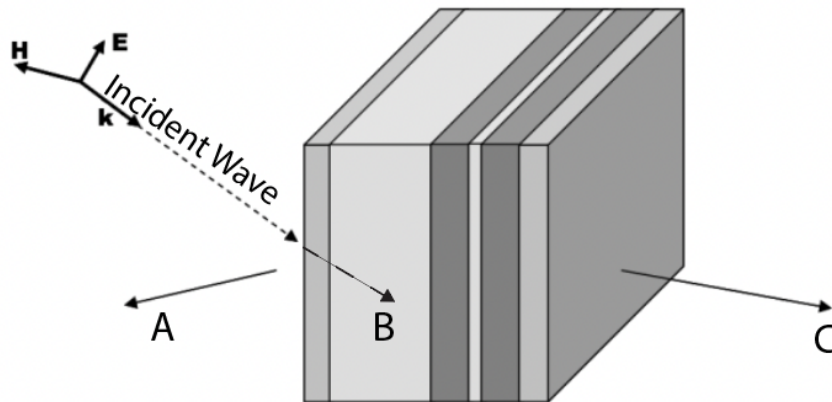
Figure 2: Depiction of an incident wave being (A) reflected, (B) absorbed, or (C) transmitted [6].

The interesting optical properties of these periodic structures are defined by several fundamental equations. Snell's law relates internal and external incidence angles to the material refractive indices.

$$\textit{Snell's Law:} \quad n_{ext}\sin\theta_{ext} = n_H\sin\theta_H = n_L\sin\theta_L \text{ [4]} \quad (1)$$

Where n_{ext} is the external medium's RI, n_H is the RI value corresponding to the high RI material, and n_L is the RI value attributed to the low RI material. Similarly, θ_{ext} refers to the external incident angle, θ_H is the internal angle of incidence for the high RI material, and θ_L is the internal angle of incidence for the low RI material. Snell's law is powerful in that it provides a fundamental description of light angle refraction at an interface between any given contacting layers. To quantify the light propagation in these multilayer structures, the transfer matrix method (TMM) used [4]. The TMM accounts for two fundamental types of propagation transformations: those observed at each interface, and the phase change associated with light traveling through a given layer. A transfer matrix mathematically relates incident and reflected light at the input and output of a multilayer structure [6]. This is done by creating a matrix for each interface (Equation 2) and the phase change from propagation through each layer (Equation 5) and then all matrices are sequentially multiplied together to obtain the propagation through the entire multilayer structure. [6]. The individual interface propagation is described mathematically by equation 2:

$$\begin{bmatrix} E_F(x_i^+) \\ E_B(x_i^-) \end{bmatrix} = \begin{bmatrix} t_{ij} & r_{ji} \\ r_{ij} & t_{ji} \end{bmatrix} \begin{bmatrix} E_F(x_i^-) \\ E_B(x_i^+) \end{bmatrix} \quad \text{(2) [6]}$$

Where i and j are given layer indices, t and r are complex transmission and reflectance coefficients as defined by Snell's law, E_F and E_B are complex propagation amplitudes, and positive and negative superscripts indicate quantities just before or after the interface [6]. This expression accounts for light that is either lost (reflected) or passed through (transmitted) at

each interface, where each interface has its own iteration of these values. Next, it is important to describe the phase change associated with propagation through a given layer *i*. The amplitudes of the propagating waves before and after the interface are described by equation 3:

$$
\begin{aligned}
E_F(x_i^-) &= E_F(x_{i-1}^+)e^{-jk_{x,i}d_i} \\
E_B(x_{i-1}^+) &= E_B(x_i^-)e^{-jk_{x,i}d_i},
\end{aligned}
\qquad \text{(3) [6]}
$$

Where d_i is the layer thickness and k_x is the x-component of the wave vector. By defining Φ in equation 4, the transfer matrix for propagation through layer *i* can be described as seen in equation 5:

$$
\Phi = k_{x,i} d_i \qquad \text{(4) [6]}
$$

$$
\mathbf{T}_i = \begin{bmatrix} e^{j\Phi_i} & 0 \\ 0 & e^{-j\Phi_i} \end{bmatrix} \qquad \text{(5) [6]}
$$

These relations yield the resulting light propagation (constructive and destructive light interference) through a multilayer dielectric structure as shown in Figure 3:
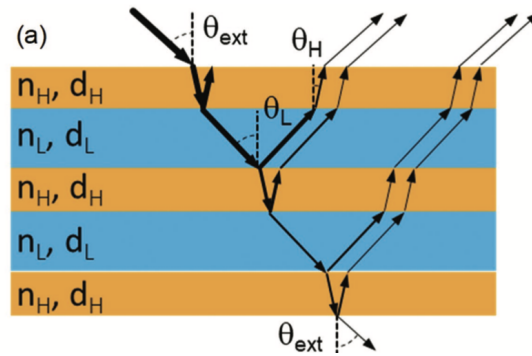
Figure 3: Demonstration of light propagation through a 1D Photonic Crystal. The n_H and d_H quantities refer to the RI and thickness of the high RI material, while n_L and d_L quantities refer to the RI and thickness of the low RI material [4]

A wide array of material systems have been identified as valid dielectric layering materials in these structures for their transparency at high-energy wavelengths, notably high or low refractive indices, and processing capabilities [4]. Typically, to manipulate the structural parameters that allow for reflectance peak location tunability while retaining the desired 90% or greater reflectance peak heights, expensive lithography or vacuum deposition processes for the dielectric materials are employed [4]. Recent efforts strive to circumvent these intensive synthetic processes traditionally used for DBR fabrication, while retaining desired functional properties. The presented study has yielded an entirely solution-processed DBR system that spans a significant reflectance peak location continuum, and possesses optical properties that make them fit for use in optoelectronic waveguiding applications . This was achieved by using PMMA as the low RI material (n = 1.49) and colloidal titania as the high RI material (n = 2.12) in a spin coating process [7][8]. Given the success of this system, current and future project efforts are focused on the incorporation of cesium lead halide nanocrystals into these devices, with the overall goal of fabricating entirely solution-processed next-generation solar devices.

1.3 Photoluminescent Nanocrystals

Broadly, the term luminescent nanoparticles (NPs) refers to a subset of chemical species consisting of any nanoscale material that possesses luminescent properties [9]. This scope includes organic species, inorganic species, biological species, and beyond. These particles are further categorized by fundamental descriptions of chemical identities, physical morphology, and quantitative photoluminescent properties. The term nanocrystal (NC) typically refers to semiconductor crystals that are colloidally grown to be between around 1 - 100 nm in size [10]. This category includes ionic perovskites: the inorganic photoluminescent nanocrystal (PLNC) of particular interest to this study. To further distinguish PLNCs from NCs, one must examine their radiative excitation and emission mechanisms. While luminescence is more broadly defined as spontaneous radiative emission from an excited species, photoluminescence specifically refers

to emission of radiation from a species experiencing direct photoexcitation [9]. Thus, the best definition given to the nanoparticles of interest to this study is photoluminescent nanocrystals: nanoscale, periodic structures that spontaneously emit radiation when subjected to direct photoexcitation.

Lead halide perovskite NCs have been identified as optimal chemical species for use in studies striving to advance the efficiency of optoelectronic devices. This is attributed to their photonic properties aligning nicely with various photovoltaic parameters and constraints. Not only are they photoluminescent, but they absorb and emit photons in distinct regimes. The absorptive and emissive properties inherent to these materials help mitigate loss due to reabsorption and rethermalization [11]. They are notable for having photoluminescent quantum yields that approach 100%, and extremely narrow emission wavelength bands [12]. Lead halide perovskite nanocrystals are also remarkable for their defect-resistant nature [13]. The presented study's further specified interest in Cesium Lead Halide ($CsPbX_3$) perovskites in particular is attributed to the stability warranted by an all-inorganic composition, relatively cheap reactant materials, and resulting compatibility with solution-processing techniques [12] [13]. The room-temperature, in-air synthesis of Cesium Lead Bromide ($CsPbBr_3$) NCs throughout the duration of this project yielded the luminophores needed to serve as the key optical cavity constituent in the later detailed DBR:Perovskite LSC architectures.

1.4 Applications

1.4.1 Luminescent Solar Concentrators

In typical solar cell operation, photons incident upon the module span a wide range of energies (with associated wavelengths) that align with the solar spectrum. Photovoltaic circuits are most efficient when photons are incident upon them at the semiconductor's bandgap energy. Only

photons with energy at or above this energy threshold are able to promote an electron from the semiconductor's valence band to its conduction band, subsequently resulting in current generation and power production. Photons incident well-above the bandgap energy experience energy loss in the form of heat dissipation. LSCs are able to tune incident sunlight via photon absorption and emission to produce photons that nearly match the bandgap energy of a given semiconductor, reducing efficiency losses.

Historically, luminescent solar concentrators (LSCs) were viewed as cheaper, less efficient photovoltaic alternatives or additions to traditional silicon solar cells. Recent studies have challenged this outdated notion entirely, and the renewed interest in these devices has been augmented by the emergence of nanocrystal luminophores: particularly their ability to mitigate reabsorption losses associated with inadequate Stokes shifts [3] [14]. These devices show promise in sufficiently increasing next-generation solar device efficiency, as they are able to tune broadband incident light to a desired wavelength, concentrate these optimized photons, and direct them to a semiconductor within a PV circuit [3]. Furthermore they are mechanically flexible, fit for use in a range of environments, and can be visually appealing if needed. Typically, photon emission is isotropic, meaning they are released in all directions evenly. In a solar circuit, it is critical that these photons be preferentially directed toward the semiconducting material, as they are otherwise lost. Thus, the structure is composed of two key components: the light absorbing and re-emitting material known as the luminophore, and the wavelength-tuned light trapping structure known as the waveguide. Both luminophores and waveguides are names given to broad categories of materials that have many constituents. LSC luminophores candidates include luminescent organic dyes, inorganic quantum dots, and the current constituent of interest: colloidal nanocrystals, specifically cesium lead halide perovskites. [3] [14]. Waveguides may be composed of organic polymers, inorganic dielectric species, and beyond. The key property is that the waveguiding mirror is largely transparent, but highly

reflective at the electromagnetic wavelengths of interest. LSC functionality is described as follows: the luminophores absorb broadband incident sunlight, and re-emit within a narrow emission band across which the waveguide is highly reflective. The waveguide then traps, concentrates and directs the re-emitted photons to a photovoltaic cell via total internal reflection (TIR) [3] [14]. This is described in Figure 4:
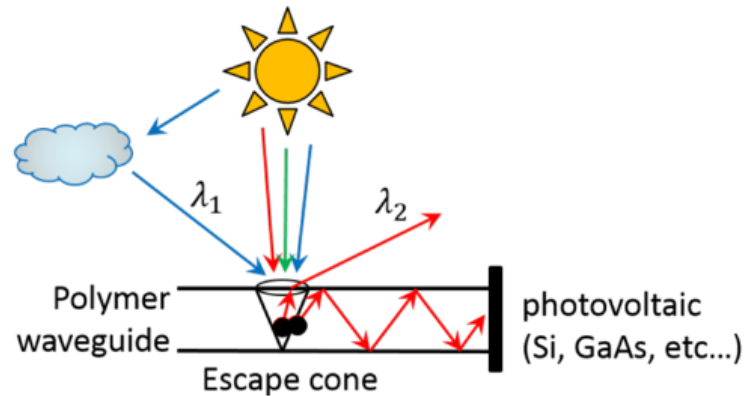
Figure 4: Diagram of an LSC waveguide. Incident broadband sunlight is absorbed by the luminophore (perovskite, CdSe, so on..) and re-emitted at the desired wavelength . The waveguide traps these re-emitted photons and directs them to the photovoltaic semiconductor via total internal reflection. The refractive index differentials between the waveguide and surrounding medium allow for most photons to be retained in the device, though some escape due to incidence at an angle within the escape cone. [14]

By sandwiching colloidally synthesized lead halide perovskite PLNCs in a cavity between two appropriate DBR mirrors, a LSC environment can be created [15]. This further specified structures is composed of an optical cavity, a dielectric material with a high refractive index, and a dielectric material with a low refractive index [4]. The dielectric materials are layered in an alternating pattern above and below the optical cavity to form the photonic DBR crystals. The refractive index difference is ideally tuned to the nanocrystal of interest, and allows for optimal light trapping and guidance along the longitudinal direction of the stack toward the solar cell semiconductor [4]. The optical cavity itself disrupts the transverse symmetry of the stack, and creates an environment in which photonic modes arise and allows for emissive coupling of photons emitted from the photoluminescent nanocrystal, as seen in Figure 5 [4]:
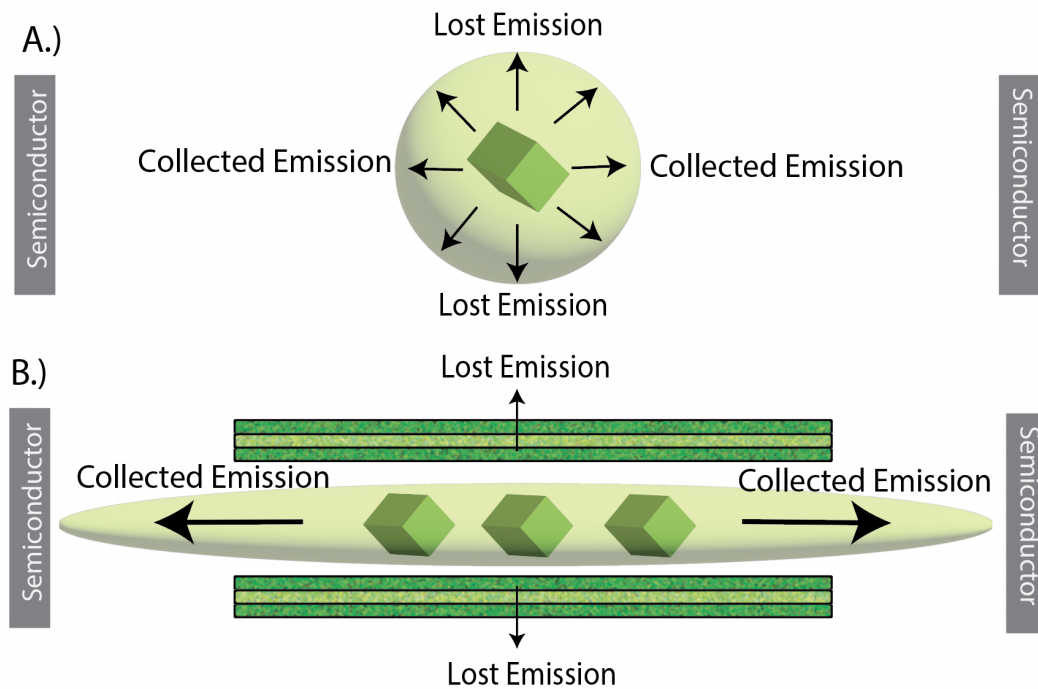
Figure 5: Depiction of A.) typical isotropic photon emission from PLNCs in most media and B.) the preferential direction of these re-emitted perovskite photons toward a collecting semiconductor when sandwiched between two DBR crystals.

The light trapping, internal reflection, and emissive coupling that arise in these DBR stack filters yields concentrated, tuned, and directionally conducted photons that optimize the activity of solar circuit semiconductors. This thesis outlines a completely solution-processed DBR waveguide system that has shown preliminary compatibility with $CsPbBr_3$ perovskite nanocrystals, thus creating the components of a novel LSC system to be optimized for use in practical solar applications.

1.4.2 Light Emitting Diodes

Light Emitting Diodes (LEDs) have garnered substantial attention in recent years for their power-saving attributes. Their characteristic function is to emit light when an electric current is passed through them. Typically they use on the order of 75% less energy than incandescent lighting, and have a 25 year lifetime extension [16]. Other advantages have given rise to

mainstream integration of these devices into several forms of everyday technology. These benefits include highly directional light emission, minimal heat dissipation, and tunable color-specific displays: all of which give further improved device efficiency and functionality. Device applications include public lighting, device displays and beyond [16]. DBR structures and PLNCs have demonstrated enhanced LED functionality in recent years.

Perovskite LEDs have seen external quantum efficiencies as high as 23.4%, and the use of these directional emitters has proven capable of increasing traditional OLED device efficiencies to 40% [17] [18]. Study of lead halide perovskites in particular indicate potential for great performance as emitters in LED applications. This notion stems from studies exemplifying control over the perovskite's angular emission through manipulation of its optical environment, particularly a reduction of its angular component [17]. The angular emission concerns the direction and strength of an electron's transfer between the ground and emissive state of an emissive material, and largely governs the optoelectronic functionality of many devices, especially LED's, LSC's, and lasers [19].

 LEDs are of particular interest to the presented study, as the DBR stacks provide cavity-surrounding dielectric environments that will largely influence this emission. Previous works have shown that placing an Al_2O_3 thin film coating atop a quantum confined $CsPbBr_3$ blue nanoplatelet assembly successfully reduced the perovskites angular emission from 30º to 14º, which translated to a 5.9% increase in external quantum efficiency for that device [17]. This established relationship between cesium lead halide perovskite angular emission and metal oxide surrounding environment is of great interest to the DBR project. By varying the Bragg mirror parameters and perovskite confinement, light propagation can be coerced through the front face of a DBR structure in LED structures, or concentrated and directed through the sides of the structure in LSC environments as seen in Figure 5. Thus, it is a goal of this work to

establish that the Titania:PMMA stacks are capable of reducing or increasing the angular emission of the synthesized nanocrystals. Because the $CsPbBr_3$ perovskites of present interest are green-emitting nanocubes, which are significantly less confined than the blue platelets in the Al_2O_3 project, the emission is inherently more isotropic. As such, the highly reflective DBR stacks embedded with the nanocrystals are hypothesized to better trap and direct the light needed in either application while utilizing the analogous metal oxide chemical environment in the prior work. Controlling $CsPbBr_3$ emission with DBR mirrors will allow for novel, efficient, and solution-processed LED, LSC, and lasing environments.

1.4.3 Lasers

The presented DBR architecture's applications in lasing applications are analogous to the LSC and LED scenarios, and are largely attributed to the system's material properties and architectural design. Understanding fundamental laser operation elucidates the role of 1D photonic crystals in these devices. In a laser, light or electrical excitation sources incident upon a gain medium promote electrons from the valence to conduction bands. When the gain medium's electrons relax to their original state in the valence band, photons are emitted [20]. These photons are trapped within the gain medium's optical cavity by surrounding mirrors that allow for the new photons to once again interact with the gain medium. In this way more gain medium electrons are promoted and relaxed, releasing even more photons into the lasing cavity [20]. This results in a cascading effect that allows for the generation of many coherent, high power photons at specific wavelengths, which are determined by the gain medium and reflective mirrors about it.

Now, the role of the DBR stacks is clear: these 1D photonic crystals possess the wavelength-specific, highly reflective optical properties needed to surround the gain medium in

these lasing applications. Literature has confirmed this notion, stating that DBR mirrors suitable

for this application should have reflectivity peaks nearing 99%, low absorption, and high

electrical conductivity [21]. The presented Titania:PMMA structure's reflectance peak continuum

has peak heights nearing this value, the architecture largely transparent, and incorporates the

conductive TiO_2 material. This project offers a simple, solution-processed bragg mirror system

whose parameters can be easily modified to generate reflectance peaks that align with lasers

across the visible spectrum. Prior polymer-polymer, solution-processed bragg stack media have

achieved suitable reflection peak spectra through as high as 128 dielectric layers per mirror [22].

Other hybrid inorganic-organic lasing DBRs achieve this functionality through more complicated

thermal-deposition processes that take place under vacuum [21]. Thus shifting towards

synthetically simple processes will be attractive for the advancement of laser technology and

increased commercial viability

1.5 Solution Processing

It is important to further develop the recurring solution-processing theme, its implications, and its

role in the current nanophotonics field. Generally in this context, solution processing refers to

the construction of optoelectronic environments by working with constituents in a solution

phase, rather than solid, vapor, or plasma. The simplistic structure of 1D photonic crystals, such

as DBR stacks, allows for these photoactive architectures to be processed in this manner [4].

This is a significant deviation from the traditional, expensive fabrication methods such as

lithography, vacuum evaporation, sputtering, and vapor deposition. While these techniques were

effective in creating the standalone, bulky, inorganic DBRs there has been a growing desire to

shift to solution-processed methods [4]. Functionally, the movement originated because the

resulting DBRs were not flexible, had poor mechanical stability, and the fabrication techniques

themselves were often severe, making it difficult to incorporate them into practical devices [4].

Economically, solution-processing is much more cost-effective, scalable, and practical for device

implementation. There are a number of solution-processing techniques that see practical use at the lab-scale, two of which are seen in Figure 6:
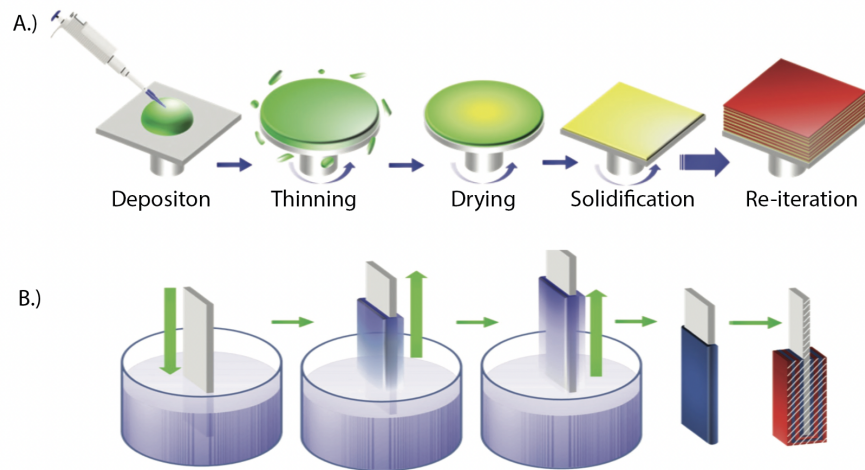
Figure 6: Depictions of A.) spincoating and B.) dipcasting solution processing techniques [4].

The solution-processing techniques, while simple in design, are subject to a wide array of chemical interactions and unforeseen complications. Of particular interest to this study is developing spincoating techniques that allow for fabrication of effective DBR photonic crystals.

Chapter 2: Individual Layer Attributes

While the application-suitable products of this work are the multilayer photonic crystal DBR stacks, it is critically important to understand the constituents that make up these structures. As such, various experimental trials were conducted to analyze the thin titania and PMMA films that create the Bragg mirrors. This chapter focuses on these individual component experiments and results, while Chapter 3 examines the multilayer DBR structures.

2.1 Colloidal Titania (TiO$_2$) Layers

Colloidal titania offers high transparency in the UV range, a large refractive index (n = 2.12), and solution-processing compatibility [4] [8]. As such, it is an ideal candidate for the high refractive

index material in the solution-processed DBR photonic crystals synthesized in this study. The following sections detail its synthesis and characterization.

2.1.1 Titania Layer Synthesis

Titania layer synthesis follows an entirely solution-processed protocol. The thin films were created on glass substrates. These were made by cutting standard FisherSci glass microscope slides down to 1 inch by 1 inch squares. The glass substrates were then cleaned with isopropyl alcohol dousing, kimwipe drying, and dust removal with a silicone air pump. This cycle was repeated until all debris and residue were removed. This protocol holds true for all substrate preparations in this study. Once the substrates were prepared, layer depositions could begin. First, a TiO_2 precursor solution was prepared in accordance with Anaya et al. [8]. Titanium isopropoxide (TTIP) was combined with hydrochloric acid and excess ethanol, then allowed to stir for at least an hour before use. Two different titania precursor solutions were created: the less concentrated TTIP1 and more concentrated TTIP2 [8]. A Laurell Technologies WS-650Mz-23NPPB spincoater was used to evenly disperse the colloidal titania solution on the glass substrate. Titania depositions were held at a constant 2000 RPM spincoating speed, and a 200uL volume of precursor solution was deposited for a single layer. These parameters hold true for both TTIP1 and TTIP2 depositions. A given deposition was allowed to spin at 2000 RPM for 30 seconds, ensuring that all solvent evaporated and left behind a thin TiO_2 film. This film was then annealed at 75ºC in a FisherBrand 120V gravity oven for 10 minutes. The heating treatment promotes titania grain growth, and anneals the material into a dense, cohesive layer. The resulting titania films are shown in Figure 7:
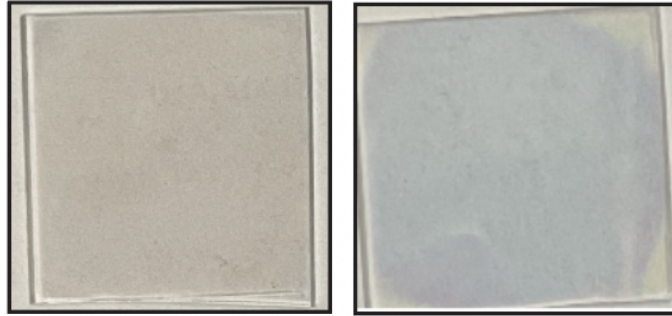
Figure 7: Images of titania films from TTIP1 (left) and TTIP2 (right) precursor solution depositions on glass substrates.

2.1.2 Titania Layer Characterization and Results

It is critically important to ascertain the thickness of each titania film, as well as all other layers that compose the multilayer photonic DBR crystals. An additional key metric to model based on experiment for the titania film layers is the effective refractive index. While the RI of titania itself is well-known for being relatively large, titania sol gel film values can vary on the order of tenths to hundredths depending on the processing techniques [8]. For example, Anaya et al. initially drew upon a literature value of 2.2 for titania, however after their DBRs were fabricated, they were instead able to back out an effective value of 2.12 for their titania films [8]. Given that the procedure used to synthesize these films is unique to this project, an effective titania film RI must be determined based upon empirical results. This can be done by first determining the thickness of the TTIP1 and TTIP2 films, then measuring the completed DBR stacks' reflectance spectra, next comparing to theoretical DBR reflectance spectra generated in the OpenFilters Software, and finally refining the RI value accordingly. OpenFilters is an incredibly powerful software tool that allows for thin film modeling via the transfer matrix method. Users can specify each layer's refractive index and thickness, and calculate the expected spectra of interest (absorbance, transmission, reflectance, etc.) [23]. It also allows for multiple layers to be stacked

upon one another and generate the same set of optical spectra for an entire filter stack, which will be done and explored more in Chapter 3.1.2 for the complete DBR crystals. Adjusting the effective RI from the empirical thin film spectra draws upon this key assumption: because layer thicknesses are experimentally determined and fixed, only optical scattering and film RI discrepancies combine to form the error observed between the empirical lab data and theoretical OpenFilters plots.

To fulfill this protocol, the individual TTIP1 and TTIP2 layer thicknesses must first be determined experimentally. First, single layers of TTIP1 and TTIP2 were deposited, spun and annealed, producing the typical even distribution on a glass substrate. Next, these films were scored with a razor blade. This made it possible to measure the film thicknesses via atomic force microscopy (AFM) on a Bruker Dimension FastScan SPM setup in UCLA's California NanoSystems Institute's (CNSI) shared space. To accomplish this, the cantilever tip is engaged near the edge of the film/razor scoring interface. Scan area parameters were programmed such that a $20um^2$ area was measured with an aspect ratio of 20. This caused the microscope to measure a 20um by 1um area, ensuring that the cantilever tip was dragged across the titania film, down the steep film/razor scoring edge, and across the glass substrate. The collected data is presented in Figure 8:
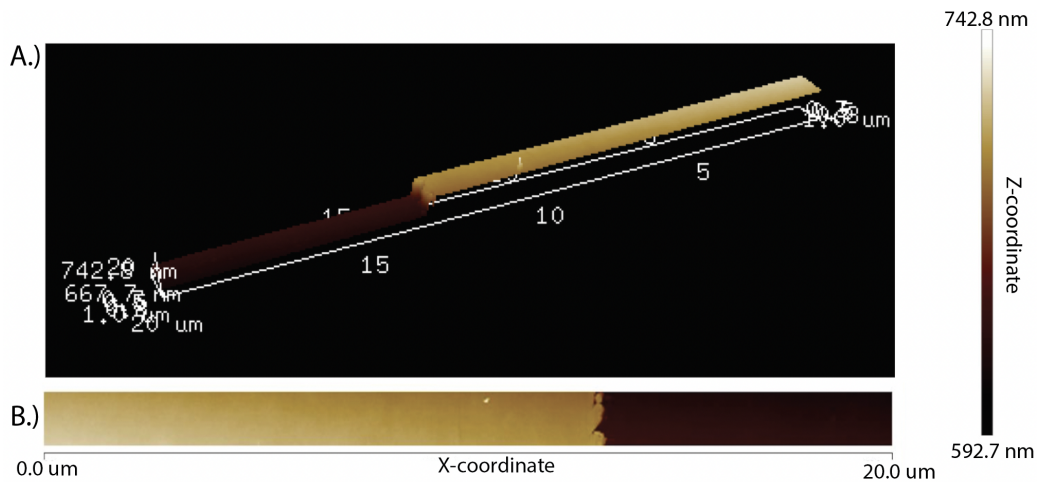
Figure 8: AFM-produced A.) 3D scan of the TTIP1 Film/Glass substrate interface and B.) height map of the same region. The scale bar is provided as well.

As seen above, the AFM data processing software produces a 3D matrix of x, y, and z position coordinates, yielding the 3D image and 2D height map. To calculate thickness, one can simply subtract the height of the titania film region from the height of the glass substrate. To find the best thickness value for each film, multiple values across an individual TTIP1 and TTIP2 sample's interface were calculated, and several films of each category were measured in this way. The data processing was as follows. First, multiple cross sections were selected for a given film of either TTIP1 or TTIP 2. An example cross section is seen in Figure 9:
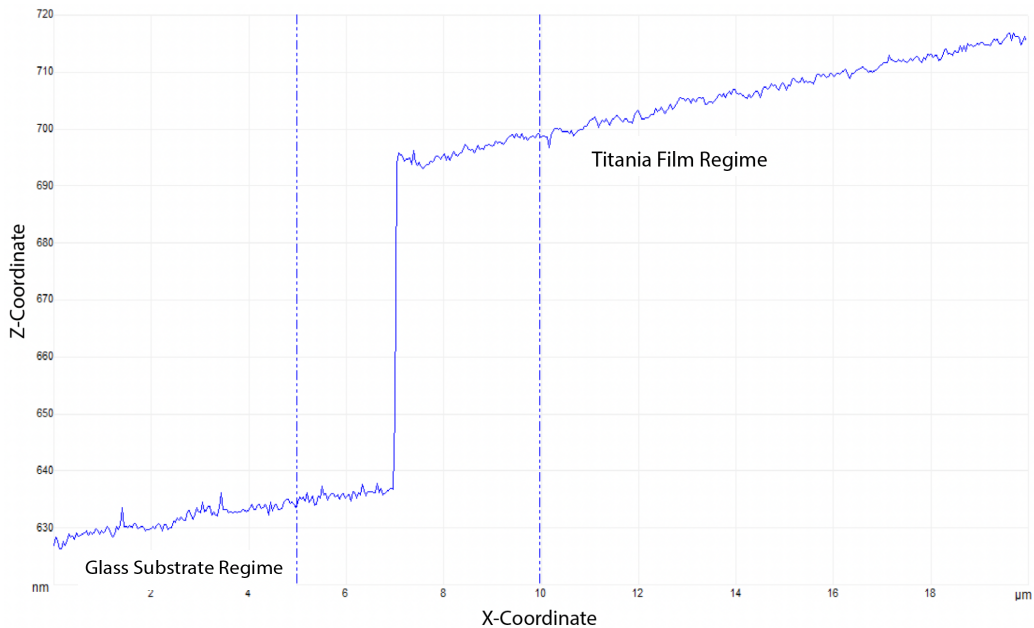
Figure 9: AFM-measured cross section of a TTIP1/Glass substrate interface extracted through the Bruker NanoScope Analysis software available at CNSI.

To correct the inherent, incredibly small slope of the glass slide substrate, a MATLAB script was written. This script takes a linear regression of the glass substrate data points (the left-hand region with a lower set of z-values before the large increase that corresponds to the edge of the film) and generates the best linear equation of fit. Then all x-values are plugged into this equation, and this generates a new set of z (height) values. Finally, the original z-values are subtracted from the corrected z-values to generate a plot that is no longer influenced by the glass substrate's innate slant. The full script is provided in Appendix A. This correction is visualized in Figure 10:
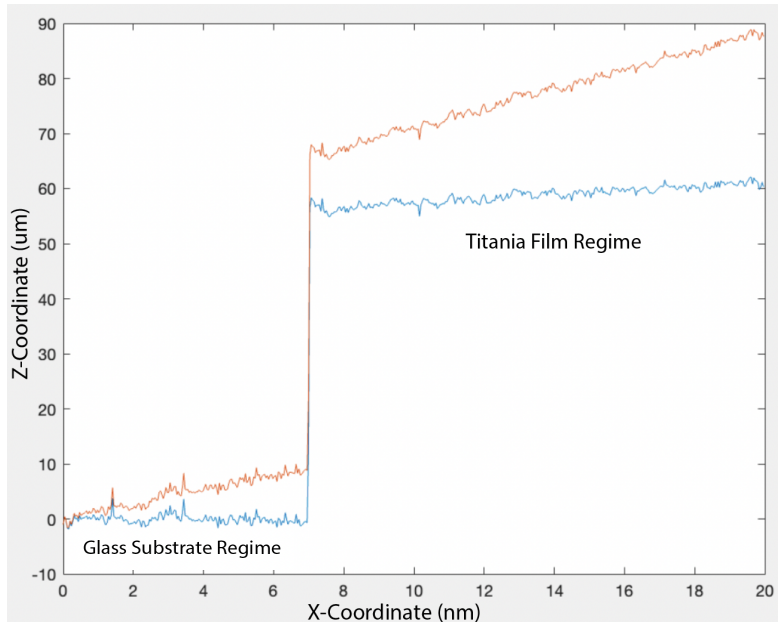
Figure 10: Slant-corrected (blue) AFM cross section of a TTIP1/Glass substrate film interface plotted against the raw experimental spectra (orange).

This same script then found the x-indices corresponding to the largest difference between two consecutive z-values, indexed both forward and backward by a user-provided integer number of indices depending on the sample, and subtracted new corresponding z-values to determine the layer thickness. This is illustrated in Figure 11:
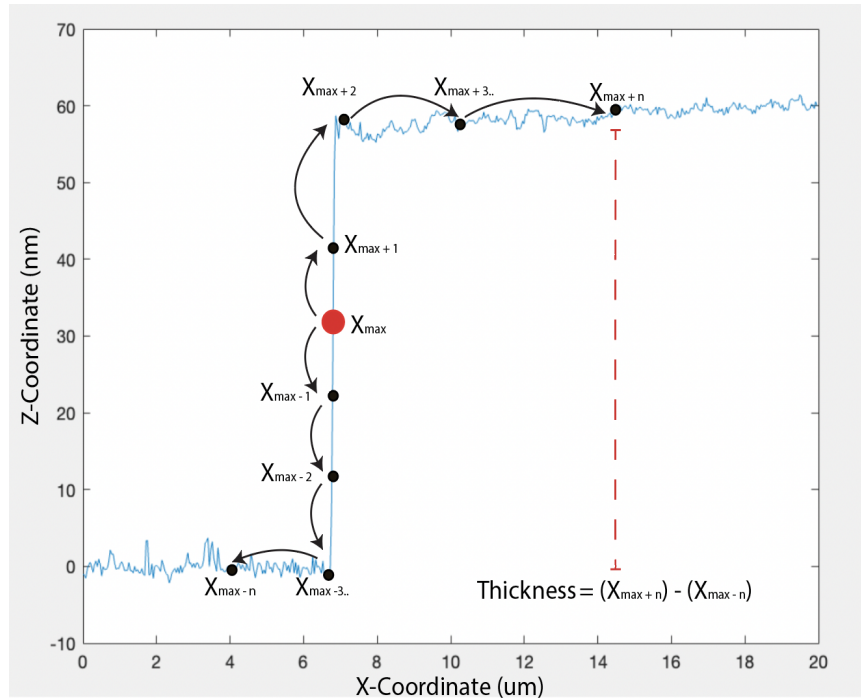
Figure 11: Pictorial depiction of the MATLAB script's procedure to determine film thickness. X_{max} represents the x-coordinate at which the maximum differential between any two z-coordinates is located. The script then traverses *n* indices in the positive and negative x-directions such that the new x-coordinates are well within the film and glass regimes. The difference of the z-coordinates that correspond to these two new x-coordinates is taken to be the film thickness.

The AFM measurements and subsequent data processing returned sensible layer thicknesses for TTIP1 and TTIP2 thin films. Average thicknesses and standard deviations are presented in Table 1:

Table 1: Titania Film Thicknesses from Atomic Force Microscopy Measurements

Titania Solution Designation	Average Thickness and Standard Deviation (nm)
TTIP1	61.22 ± 3.63
TTIP2	84.67 ± 5.42

These results affirm that the titania films are suitable for DBR stack fabrication. They are evenly-distributed, largely transparent, and on the order of tens of nanometers thick. This last detail assures that the complete 15-layer stacks that include the polymer low RI layers will be

sufficiently thin (on the order of micrometers) for implementation in real solar modules. With the thicknesses of each type of titania film solidified, the effective RI was determined for these constituents. This was done by first creating a titania film on a silicon wafer using the TTIP2 solution, and measuring its reflectance with a R600-8-UV VIS-NIR reflectance/fluorescence probe mounted on an RPH2 reflectance probe holder, both of which are products of StellarNet. A StellarNet SL5 Deuterium + Halogen light source was used to illuminate the sample This is shown in Figure 12:
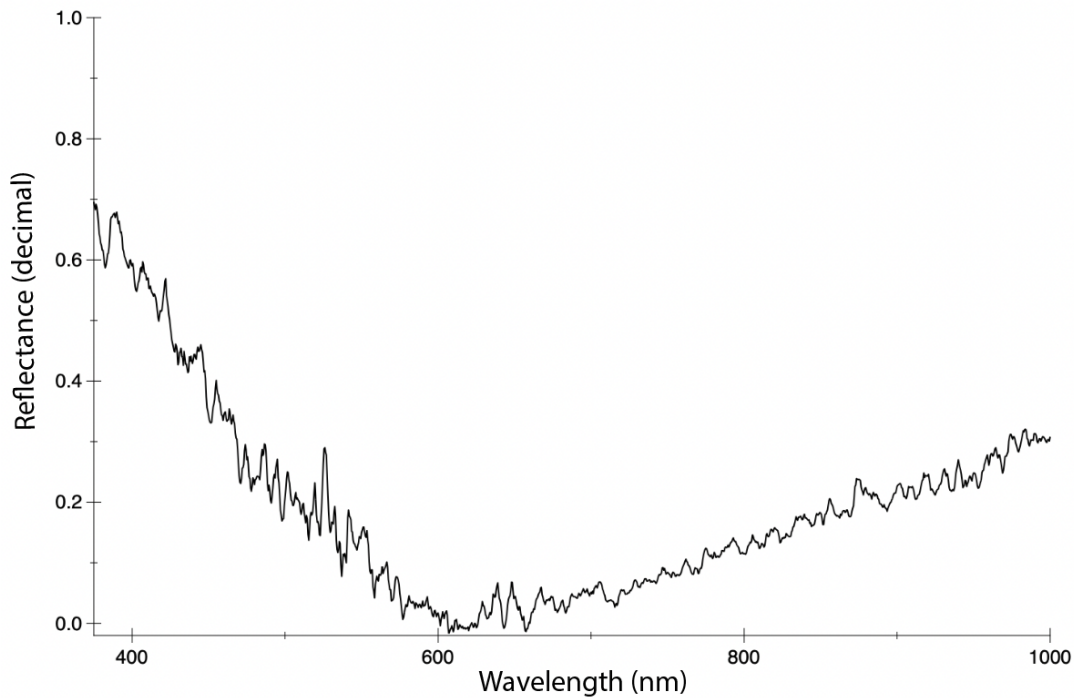
Figure 12: Reflectance spectrum of a titania film produced by a TTIP2 precursor solution.

Due to equipment limitations the titania reflectance spectrum is noisy. This is because the light source oversaturates the reflectance probe, and can only produce meaningful spectra when the minimal integration time of 1 millisecond is employed. To ensure that the probe was able to produce meaningful curve shapes, several titania films were produced from several different RPM and TTIP solution concentration combinations to capture films corresponding to various

titania film thicknesses. These were then compared to the computational OpenFilters plots, which are all available in Appendix B. Through this line of testing, it was confirmed that this film reflectance spectra was sufficiently accurate for the purposes of capturing general reflectance curve shape, and optimizing the effective RI of the TTIP2 solution's films, which are used as the high RI material constituent in the eventual DBR continuum discussed in Chapter 3. At this point, AFM measurements had experimentally fixed the TTIP2-produced TiO_2 film thicknesses at 84.67nm, and the empirical reflectance spectrum had been generated. OpenFilters was used to produce the theoretical reflectance spectrum for a 84.67nm thick titania film with the constant 2.12 RI found for these films in literature [8]. The comparison of this theoretical and experimental curve is shown in Figure 13:
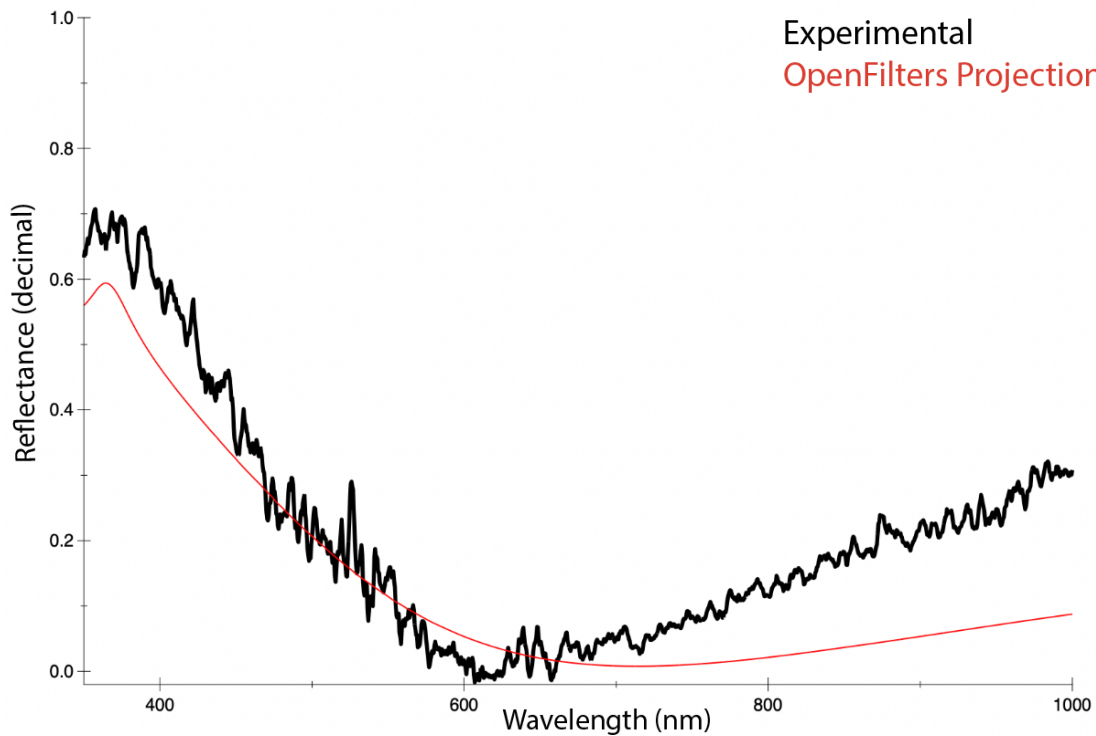
Figure 13: Comparison of reflectance spectra generated in OpenFilters (red) for a 84.67nm film programmed with a constant 2.12 RI and the experimental reflectance spectra of a titania film produced by a TTIP2 precursor solution (black).

While the general shapes are consistent, it is clear that the constant n = 2.12 model for the

titania film RI is insufficient. Furthermore, the large difference in tail behaviors between each plot

(roughly 625nm and onward) show large discrepancies that have been instead attributed to

scattering rather than RI modeling issues. To design a better RI model for this system as a

function of wavelength, only the 450-625nm domain was considered. Several theoretical

OpenFilters plots were generated using constant refractive indices beginning at 1.7 and

increasing in increments of 0.05 up until 2.2. The literature film RI value of 2.12 was also

considered in addition to each of these values. Each of these plots alongside the experimental

spectra are shown in Figure 14:
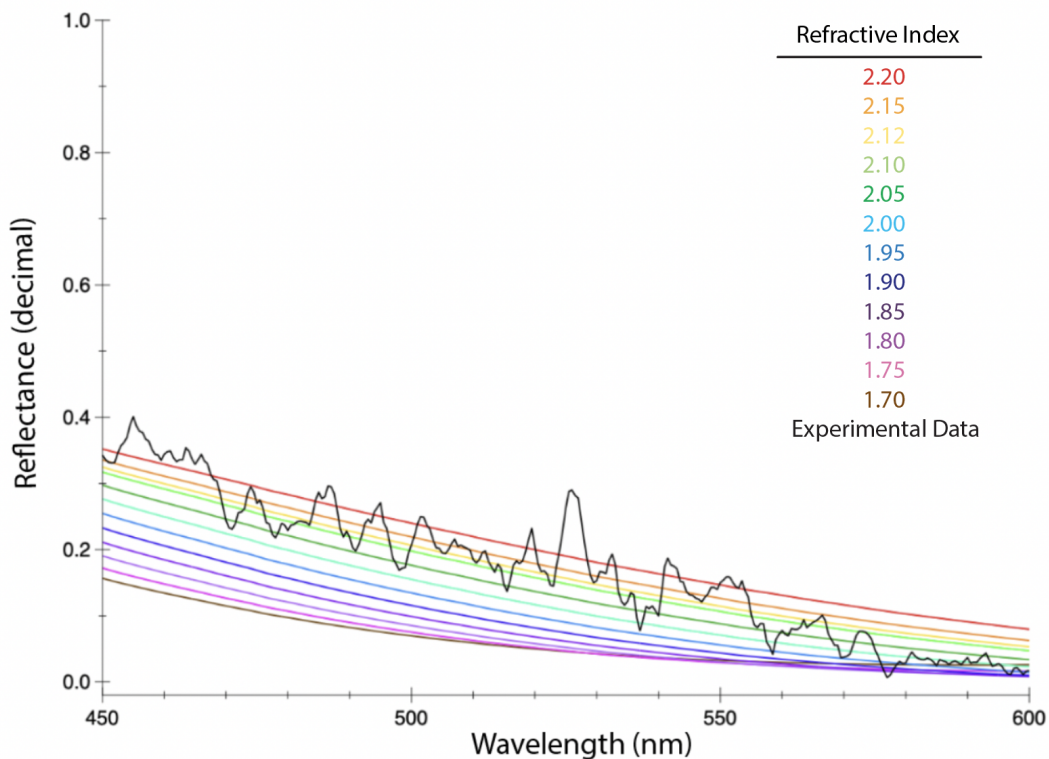
Figure 14: Empirical 84.67nm thick titania film reflectance (black) overlaid with several
TMM-generated reflectance plots in OpenFilters (colorful) of the same thickness. These colorful
TMM plots each use a different, constant refractive index constant that gradually increase by
increments 0.05 between 1.7 and 2.2. The literature value constant for 2.12 was also used to
generate a colorful plot and is included.

It is well known and expected that refractive indices for most materials are not constant, and

instead will decrease as wavelength increases [24]. This is attributed to the way incident

photons with varying characteristic wavelengths interact with materials. These wavelengths vary

inversely with energy as shown in equation 6:

$$E = \frac{hc}{\lambda} \quad (6)$$

Where E is energy, h is Planck's constant, c is the speed of light, and λ is wavelength. Materials

interacting with incident light will return different optical responses. Reflection is determined by

the way electrons in a material experience each photon's characteristic energy, and move in

response to it [24]. At lower energies, or higher wavelengths, it is more difficult to generate a

reflectance response from materials. In this way it is expected that RI will decrease with

increasing wavelength, and this phenomenon is widely observed and accepted in the photonics

field. This relationship between RI and wavelength, coupled with the plots in Figure 14 were the

principles upon which the new effective titania RI film was built upon. To better approximate the

real system synthesized in lab, the effective RI was optimized using a chi-squared (χ^2) test. This

test is generally used to determine if there is a statistically significant difference between

expected and measured data. It is employed here in such a way that it yields the best fit of a

theoretical OpenFilters curve to the collected empirical DBR reflectance spectra. The

mathematics can be expressed in words as the difference between the theoretical and empirical

spectra squared, divided by the theoretical data [19]. This expression is written mathematically

as follows:

$$\chi^2 = \frac{(theoretical\ data - empirical\ data)^2}{theoretical\ data} \quad (7)\ [19]$$

The minimum chi-square value (X^2_{min}) then corresponds to the best fit between the two curves.

Error is quantified with the alpha (α) value, which is defined as the difference between χ^2 and

X^2_{min}. An alpha value of one indicates one sigma, and a confidence region of 68% [19]

$$\alpha = \chi^2 - X^2_{min} \quad (8)\ [19]$$

25

The measured and simulated spectra were fit to one another via a chi-square test for every 25nm of the 450-625nm regime. The RI value corresponding to the X^2_{min} for each regime was then taken to be constant for its respective domain. Because RI is known to decrease with wavelength, the X^2_{min} value for the preceding 25nm regime was used as the upper bound for each sequential chi-square testing increment. The results of this analysis are shown in table 2:

Table 2: Chi-squared Values for Titania Film RI Optimization

Wavelength Regime (nm)	Refractive Indices											
	1.70	1.75	1.80	1.85	1.90	1.95	2.00	2.05	2.10	2.12	2.15	2.20
450-475	15.20	12.03	8.93	6.27	4.18	2.63	1.55	0.85	0.43	0.33	0.22	**0.16**
475.5-500	13.56	11.17	8.33	5.68	3.57	2.04	1.03	0.46	0.21	**0.17**	0.18	0.32
500.5-525	17.39	15.90	12.69	9.06	5.90	3.50	1.87	0.87	0.35	**0.24**		
525.5-550	19.98	21.11	18.64	14.13	9.58	5.98	3.47	1.89	1.00	**0.80**		
550.5-575	7.09	9.69	10.22	8.22	5.29	2.88	1.37	0.61	**0.40**			
575.5-600	0.17	0.53	1.15	1.31	0.76	0.25	**0.15**					
600.5-625	1.69	1.26	1.09	1.16	1.16	**1.06**						

Here, the best value for each interval is bolded. A sample α-value confidence interval plot for the 475.5-500nm regime is provided in Figure 15:

Chi-Squared Values
68% Confidence Inteval
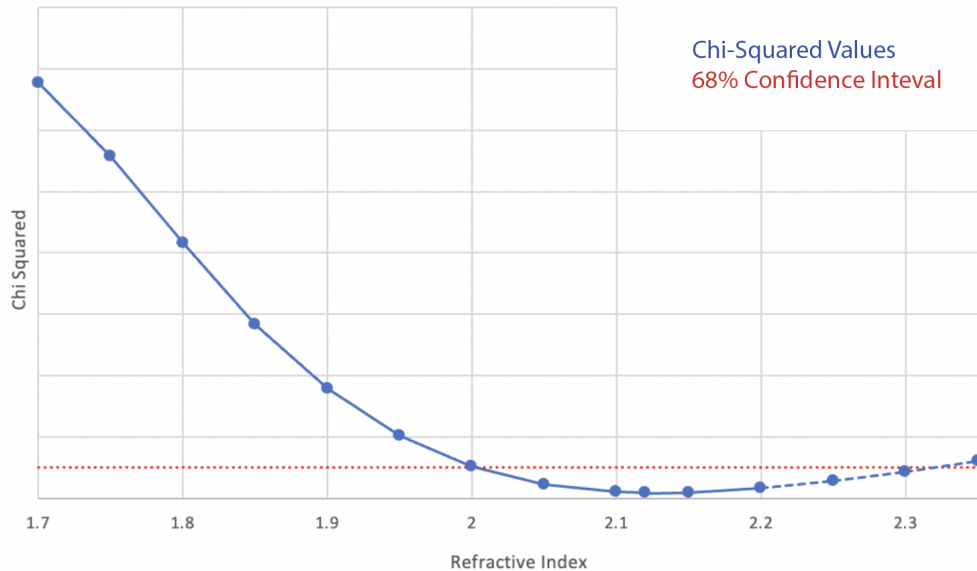
Figure 15: Chi-squared values for the 475.5-500nm domain (blue) with linear interpolation between points. The chi-squared = 1 line (red) illustrates the 68% confidence interval for this test. The dashed blue segments represent physically insignificant intervals tested to complete the confidence interval.

Figure 15 shows that 2.12 is X^2_{min} and thus the best effective RI value for the 475.5-500nm

interval, and that this value falls within the 68% confidence interval. The MATLAB Curve

Fitting Toolbox was then used to generate a polynomial function to fit this data:
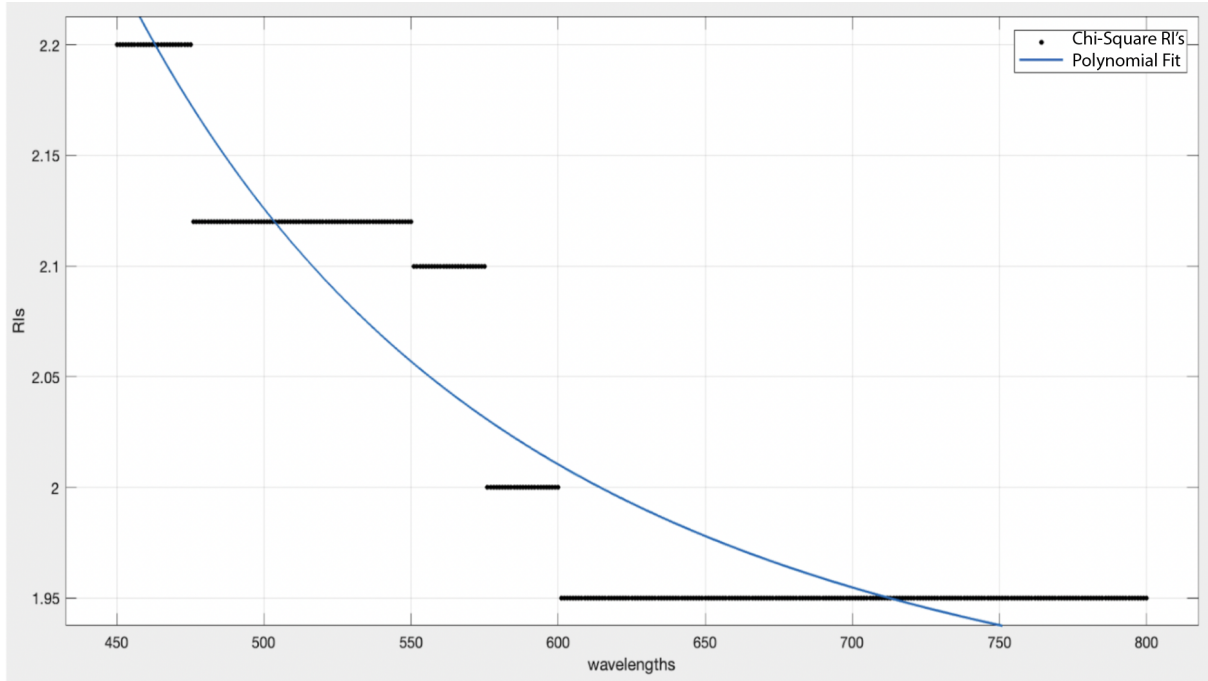
Figure 16: Using MATLABs Curve Fitting Toolbox to fit a polynomial (blue) to the X^2_{min} data generated for each 25nm regime (black segments).

This polynomial fit was optimized to the following form:

$$RI(\lambda) = A + \frac{B}{\lambda^k} \quad (7)$$

Where *A*, *B* and *k* are constants determined by the curve fitting tool with 95% confidence

bounds. Their values are shown in table 3:

Table 3: Constants for Effective Titania Film RI Polynomial Fit

A	1.872
B	$2.382 \cdot 10^8$
k	-3.324

With these constants now determined, the expression for effective titania film refractive index as a function of wavelength is written as:

$$RI(\lambda) = 1.872 + \frac{2.382 \cdot 10^8}{\lambda^{-3.324}} \quad (8)$$

This function was programmed into OpenFilters as the refractive index of a custom material that was representative of the titania films used throughout this project. The resulting spectra for this custom material, reproduced constant RI projections shown in Figure 14, and the experimental data for the 84.67nm titania film are shown in Figure 17:
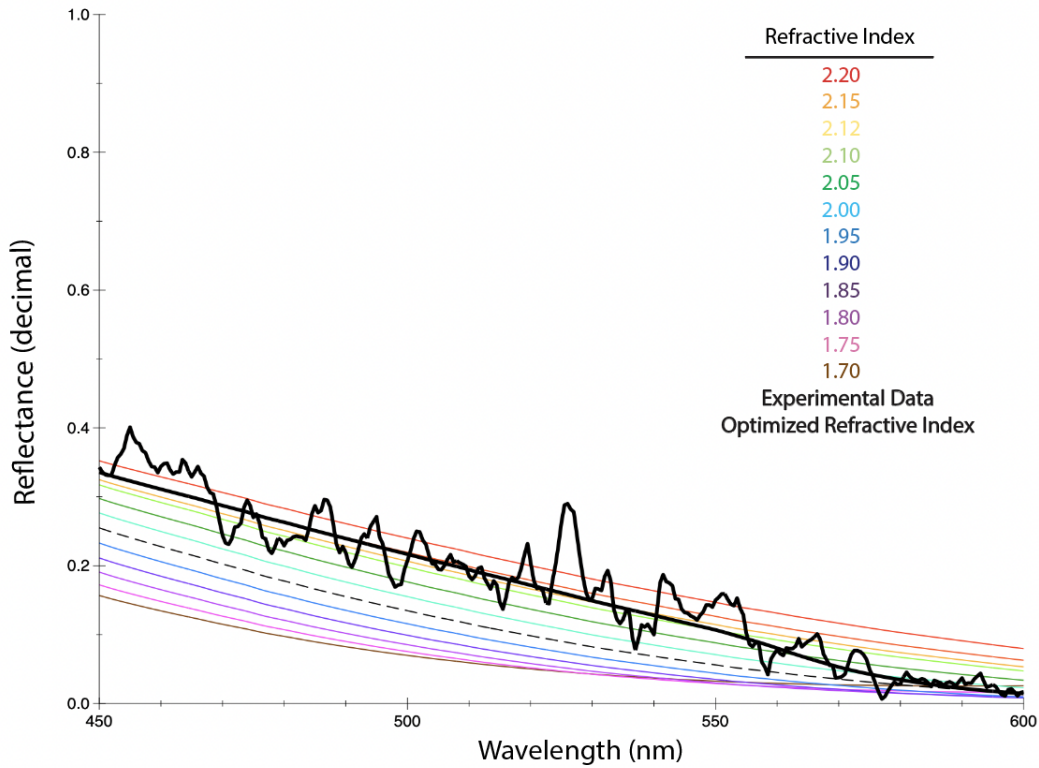
Figure 17: Empirical 84.67nm thick titania film reflectance (black), overlaid by several TMM-generated reflectance plots in OpenFilters (colorful), and the new spectra generated by the polynomial-generated RI values (also black) of the same thickness. These colorful TMM plots each use a different, constant refractive index constant that gradually increases by increments 0.05 between 1.7 and 2.2. The literature value constant for 2.12 was also used to generate a colorful plot and is included.

This exercise generated an effective RI for the titania sol gel films used in the multilayer DBR structures. Rather than approximating with constant literature values, this value can now be modeled as a polynomial that aligns with key photonic light-material interaction principles, and is backed by a 68% chi-squared confidence interval. This function produced a reflectance spectra for a single titania layer that offers a much better fit than any of the constant projections, as seen in Figure 17. This effective RI model also produced considerably more accurate multistack projections, as seen in chapter 3 and Appendix C.

2.2 Polymethyl Methacrylate (PMMA) Layers

PMMA layers are used as the low RI material in the DBR stack architecture. Like titania, it is highly transparent and solution processing compatible. It also offers sufficiently large RI contrast when coupled with titania solidifying it as an ideal constituent in this role.

2.2.1 PMMA Layer Synthesis

Similar to the titania layer syntheses, the PMMA films were formed through preparing precursor solutions and spincoating them on glass substrates. These substrates were created and prepared according to the same protocol detailed in section 2.1.1. Three PMMA solutions of varying concentration were used throughout this project: $10.03\frac{mg}{mL}$, $20.06\frac{mg}{mL}$, and $40.12\frac{mg}{mL}$. These solutions were created by adding the appropriate amounts of PMMA for a given solution to 20mL of toluene. These were then allowed to stir overnight at 60ºC, ensuring the polymer beads were completely dissolved. Multiple concentrations were used intentionally, as it was immediately apparent, and later empirically determined, that PMMA precursor concentration played a critical role in resulting layer thicknesses. PMMA film thickness is the key independent variable in DBR reflectance peak location tunability in this study, thus solution concentration and RPM variations were coupled to achieve sufficient control of these values. Depending on

desired layer thickness, one of the three solutions was spun on a glass substrate between 2000

and 6000 RPM for 30 seconds, ensuring that the polymer was set and all solvent was

evaporated off. All polymer solution films were made with 150uL of stock solution for a given

deposition. The samples were then treated in the same for 10 minutes at 75ºC to mimic the

thermal treatment these films experience when incorporated in complete DBR stacks.

2.2.2 PMMA Layer Characterization and Results

The single key experimentally-determined metric for the PMMA films was the thicknesses that

resulted from all spincoating RPM and precursor solution concentration combinations that

warranteed successful DBR stack production. Unlike colloidal titania films, the refractive index of

PMMA is well-documented and fairly consistent in most protocols. This value is typically cited as

1.5 in low wavelength regimes, and gradually falls to 1.45 as wavelength increases from 300nm

to 1700nm [21]. This data can be directly programmed into OpenFilteres as a set of ordered

wavelength, RI pairs. Thus, it was determined that the procedure for determining the effective

titania film refractive index detailed in section 2.1.2 was unnecessary for these layers, and the

literature values were sufficiently accurate for theoretical modeling. The PMMA film thicknesses

were determined in an identical manner to the titania layers: each finalized film was scored with

a razorblade, creating two distinct film and glass regimes, and allowing for accurate AFM

analysis on CNSI's Bruker Dimension FastScan SPM microscope. Once again, the cantilever tip

was engaged near the edge of the film/razor scoring interface and a 20um^2 area was measured

with an aspect ratio of 20. Like before, the cantilever tip was dragged across the PMMA film,

down the steep film/razor scoring edge, and across the glass substrate. This provided an x, y, z,

coordinate height map of the 20um by 1um area, much like the titania films. The collected data

for a given PMMA film is provided in Figure 18:
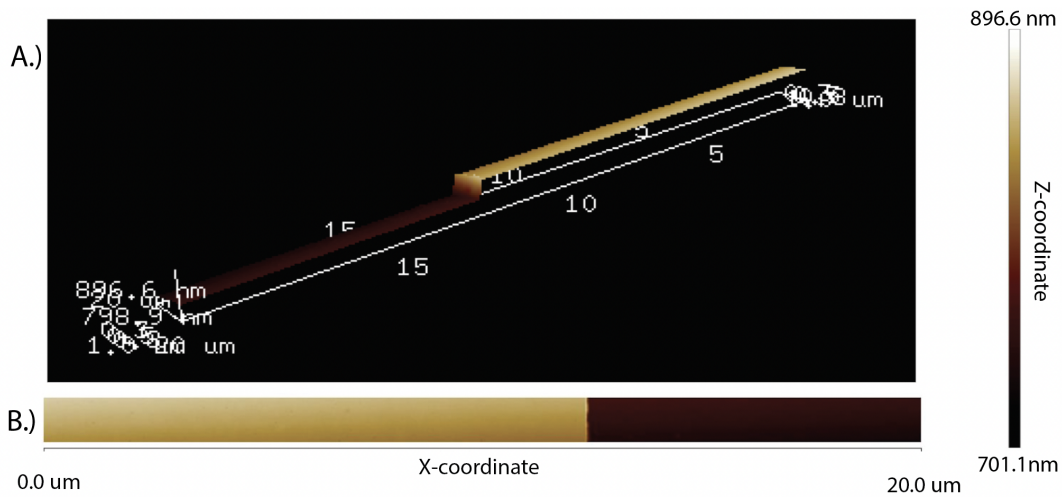
Figure 18: AFM-produced A.) 3D scan of the PMMA film/glass substrate interface and B.) height map of the same region. The scale bar is provided as well.

The collected data was processed in the same manner as the titania films. Multiple cross sections of each height map were extracted for each given sample, and several identically synthesized films were produced and measured for each set of parameters. These were then averaged and fit with a standard deviation to give an accurate range of thicknesses for each combination of film synthesis parameters. As seen with the titania films, inherent glass slide slopes were corrected using the MATLAB script detailed in section 2.1.2. A sample cross section that has been appropriately corrected for the PMMA film shown in Figure 18 is provided in Figure 19:
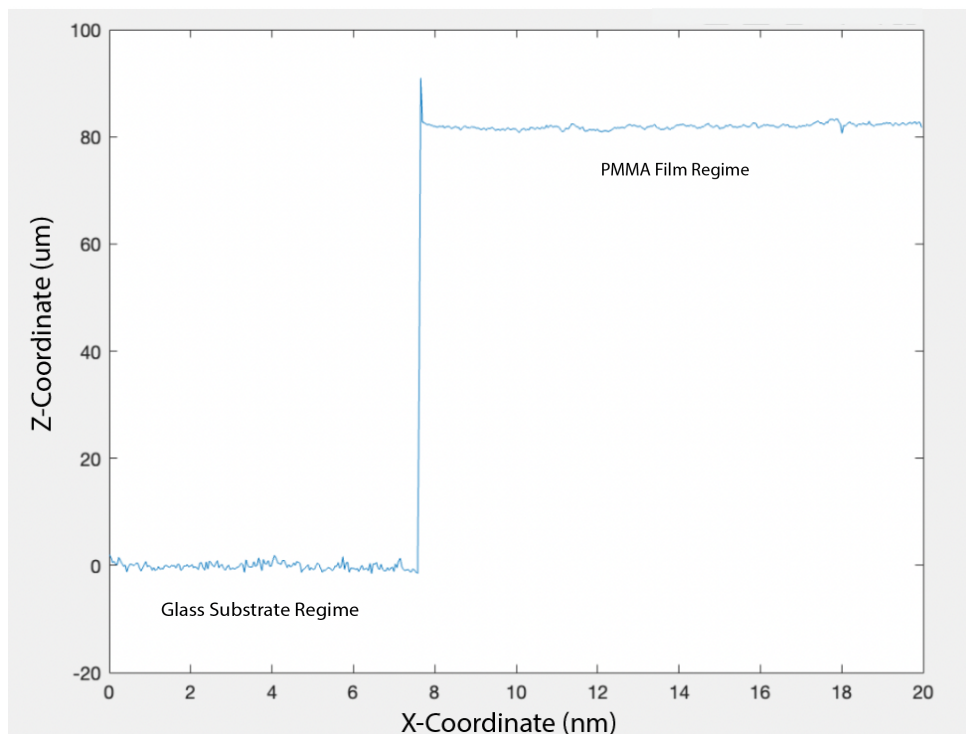
Figure 19: Slant-correct AFM cross section of a PMMA/Glass substrate film interface.

The same script, like before, also found the x-indices corresponding to the largest difference between two consecutive z-values, indexed x-coordinates in both directions as needed for each sample, and subtracted new corresponding z-values to determine the layer thickness. The number of index iterations in the x-direction was chosen such that the selected z values were sufficiently within the homogenous region of each film, and avoided any roughness or irregularities generated by the razor near the interface. In this way, all PMMA solution concentration and spincoater RPM speed combinations for each PMMA film were empirically measured. These results are compiled and presented in Table 4:

Table 4: Titania Film Thicknesses from Atomic Force Microscopy Measurements (nm)

Spincoating RPMs

PMMA Conc. (mg/mL)	2000 RPM	4000 RPM	6000 RPM
10.029	59.82 ± 1.79	40.66 ± 1.54	34.10 ± 2.59
20.058	83.41 ± 0.98	59.43 ± 2.93	50.10 ± 2.93
40.12	180.09 ± 7.30	131.83 ± 2.06	108.12 ± 1.21

The results are sensible and follow expected trends. Each layer thickness is on the order of tens to hundreds of nanometers, ensuring that the overall DBR stacks that contain these low RI layers will be sufficiently thin and compatible with real solar devices. Increase in PMMA solution concentration and decrease in spincoater RPM produced thicker samples. Conversely, decreasing PMMA solution concentration and increasing the rotational speed produced thinner layers. The maximum thickness is measured as roughly 180nm for for the $40.12\frac{mg}{mL}$ solution layers spun at 2000 RPM, while the thinnest film was determined to be about 34nm thick and corresponded to the $10.03\frac{mg}{mL}$ PMMA solution processed at 6000 RPM. This trend is visualized in Figure 20:
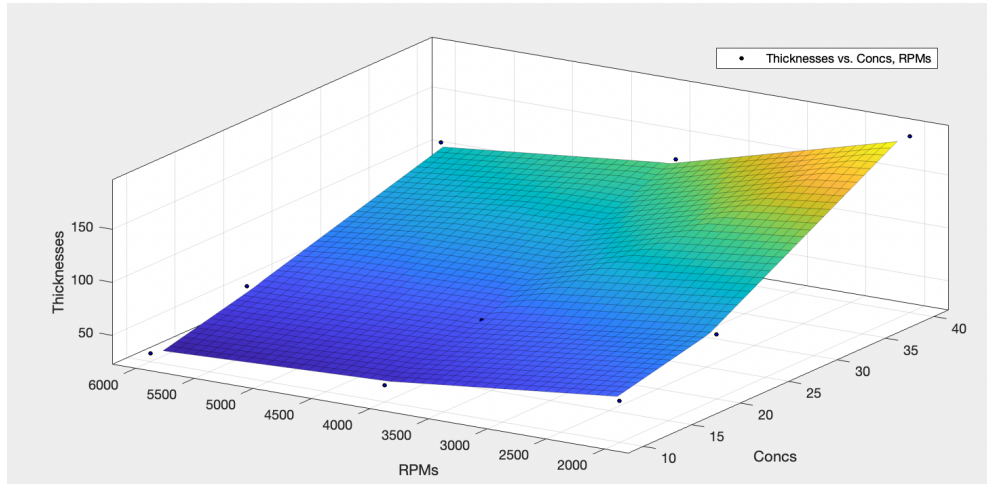
Figure 20: 3D Fitted Surface for Measured PMMA Layer Thicknesses

The fitted surface shows excellent control over the PMMA film thicknesses. By combining different PMMA solution concentrations and spincoating RPMS, any values within the 34nm and 180nm thickness extrema are attainable with relative ease. This continuum-like behavior is helpful for tuning DBR reflectance peak location, which is demonstrated in Chapter 3. By tracing any given concentration parallel (concentration held constant) or RPM parallel (RPM held constant), an interesting phenomena presents itself. While both variables influence film thickness, the larger slopes associated with RPM parallels demonstrate that, for this system's tested data points, changes in concentration have larger influence over resulting film thickness than changes in RPM. Furthermore, this trend is more pronounced for lower RPM values. These measurements and key takeaways were critically important to design and fabrication of the DBR stack continuum presented in Chapter 3.

Chapter 3: Multilayer Distributed Bragg Mirrors and Microcavities

Structurally sound, functional, and solution-processed DBRs are the one-dimensional photonic crystals that constitute the primary synthetic goal of this study. The ideal optical property of these environments is high transparency at most electromagnetic wavelengths, with the exception of a narrow wavelength regime in which they are highly reflective. Structurally they must be periodic, flexible, and sufficiently thin. This chapter details the synthesis and characterization of these multilayer structures, as well as preliminary attempts and results for nanocrystal microcavity development. Ease of fabrication is one of the paramount accomplishments of this study. As such, all DBR fabrication is achieved through a solution-processed spincoating procedure. They are composed of the individual layer constituents discussed thoroughly in Chapter 2. Two types of multilayer structures were created. First: the 15-layer DBR photonic crystals that do not contain a perovskite nanocrystal emissive layer (Cavity-Free). These are the main focus of this study, and have yielded the desired reflectance spectra continuum. Next, preliminary microcavities that do contain an emissive layer have also been produced. Stabilizing these cavities will allow for future DBR stack embedment. The synthetic procedure and optical property results for both types of structures are detailed further here.

3.1 Cavity-Free Distributed Bragg Reflectors

Cavity-free distributed bragg mirrors refer to the alternatively layered dielectric stacks that do not contain an emissive layer that breaks its transverse symmetry. The cavity-free DBR photonic crystals discussed here operate solely as waveguides, which are applicable in lasing, LED, and amplifier devices as well.

3.1.1 Cavity-Free Distributed Bragg Reflector Synthesis

The cavity-free DBRs are composed entirely of the individual titania and PMMA layers detailed in Chapter 2. The synthesis of each individual layer is the same, but now high RI and low RI films are stacked alternatively on top of one another. Again, the same glass substrates are prepared and used. First a concentration for the titania solution is selected: the less concentrated TTIP1 or the more concentrated TTIP2. Then a PMMA solution concentration of $10.03\frac{mg}{mL}$, $20.06\frac{mg}{mL}$, or $40.12\frac{mg}{mL}$ is chosen. The synthesis begins with a 200uL deposition of TTIP solution, which is spun on the spincoater for 30 seconds at 2000 RPM. This is then treated in the same FisherBrand for 10 minutes at 75ºC. Next, 150uL of the PMMA solution is dropped on top of the now heat-treated titania film, and spun for 30 seconds on either 2000, 4000, or 6000 RPM depending on desired thickness. A new titania layer is then deposited on top of the polymer layer, and subsequently treated in the oven like before. This process is repeated until the desired number of layers is attained. The cyclic multilayer protocol for cavity-free DBRs is described visually in Figure 21:
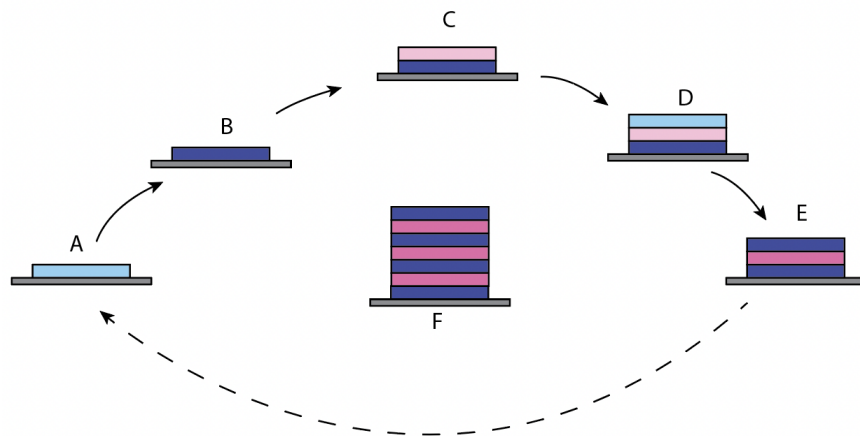
Figure 21: DBR fabrication schematic. First a TTIP precursor solution is deposited onto a substrate (A) to create a titania film, and then treated in a 75ºC oven for 10 minutes (B). A PMMA film is then deposited (C) followed by a second titania deposition directly on top of it (D). This stack is then treated in the oven again (E). This cycle is repeated any number of times until the desired number of periods is deposited on top of one another (F). [8]

Within each DBR stack, all layers of a given chemical species were held at as close to uniform thickness as possible by keeping the deposition parameters for each constant. In the upcoming continuum, the TTIP2 solution concentration was selected and spun at 2000 RPM for each individual titania layer. Unlike the PMMA solutions, this TTIP2 concentration was held constant across all stacks so as to produce the same 84.67nm film in every sample. Once one of the three PMMA solution concentrations was selected for a DBR, it was consistently deposited at either 2000, 4000, or 6000 RPM for each film in that given stack. The ideal outcome was equivalent titania thicknesses in all cases, and equivalent PMMA thicknesses within each individual stack. These PMMA values can vary between stacks to move the reflection peak position by selecting different deposition parameters, namely precursor concentration and spincoater RPM. Slight variations in each type of film thickness were expected and measured, as this procedure is susceptible to user inconsistencies.

3.1.2 Cavity-Free Distributed Bragg Reflector Characterization and Discussion

The cavity-free DBR stacks aspired to attain a location-tunable reflectance band, with peak heights on the order of 90% reflectance or greater through the presented solution-processed protocol. While 90% was the idealized peak height target, values at 85% or greater were regarded as sufficiently close to this goal and counted as successful. This is attributed to the 85% peak height nearing the lower operational bound in practical LSC operation [25]. To quantify the properties of each stack, transmission measurements were taken using the StellarNet BLACK-Comet C-SR-50 Spectrometer coupled with the StellarNet SL5 Deuterium + Halogen light source. This was connected to a transmission setup constructed from ThorLabs CP33 cage plates, a ThorLabs CBB1 Cage System U-Bench, and StellarNet F600-UVVIS-SR fiber optic cables. The transmission spectra were then transformed to reflectance spectra according to the following expression:

$$R = 1 - T - A \quad (8)$$

Where R is reflectance, T is transmission, and A is absorbance. These insulator stacks are highly transparent and have negligible absorption capabilities. Therefore, equation 8 can be rewritten as:

$$R = 1 - T \quad (9)$$

This relation was programmed into a MATLAB script that allowed for transformation of transmission spectra into reflectance spectra. With the data processing now standardized, the first focus became attaining 90% reflectance peak heights. Literature has demonstrated that increasing the number of films in a given stack yields a taller, narrower reflectance peak that shows a slight red-shifting as each pair of high RI and low RI layers are added [8] [26]. It was therefore hypothesized that bilayers could be added to the mirrors until the 90% threshold was reached. To test this, 7-layer DBR stacks were created and had their transmission spectra measured. If, after transforming the data, the resulting reflectance peak height remained below 90%, another high-RI:low-RI material pairing was deposited on top of the existing stack. This process was repeated until the peak height reached the 90% target. Nine DBR filters were produced for the finalized continuum, and are designed using the letters A-I. Figures 22 and 23 demonstrate the evolution of the reflectance spectra as bilayers were added for two exemplary samples DBR-I and DBR-G respectively:
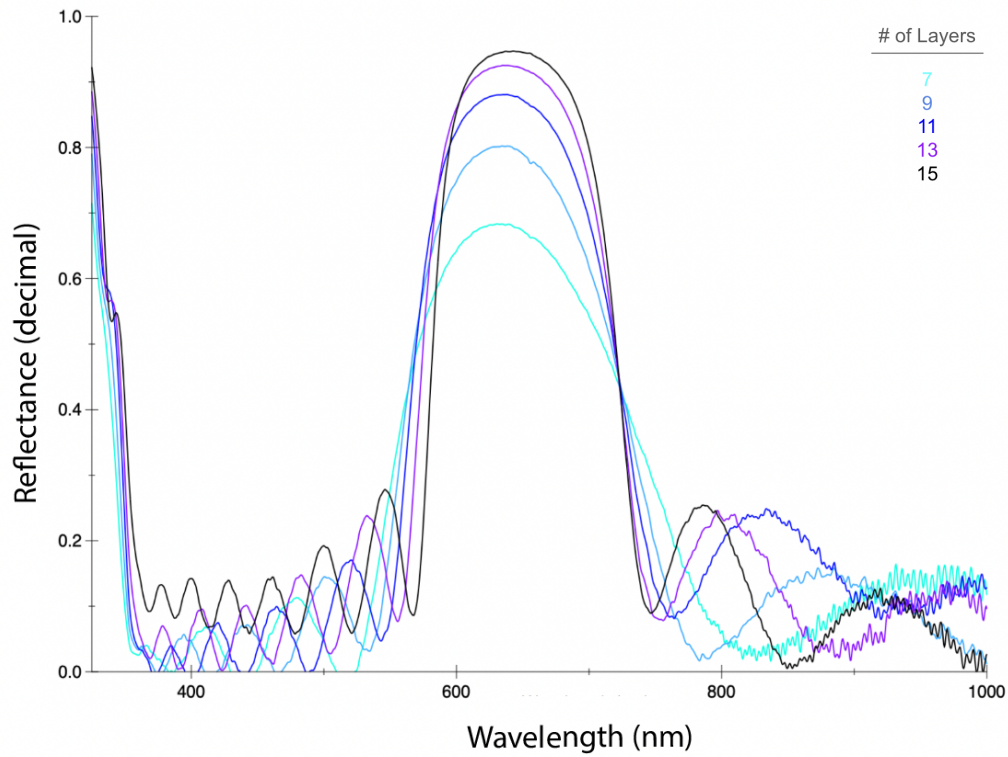
Figure 22: Reflectance spectra progression for DBR-I. Table 5 contains the key data points from these spectra.

The key data points from these spectra are contained in Table 5:

Table 5: Key Reflectance Data Points for DBR-I Layering Progression

# of Layers	Peak Location (nm)	Peak Height (%)
7 Layers	624.5	68.3%
9 Layers	628.5	80.2%
11 Layers	632	88.1%
13 Layers	629.5	92.5%
15 Layers	637	94.7%

The analogous spectra for DBR-G are provided in Figure 23:
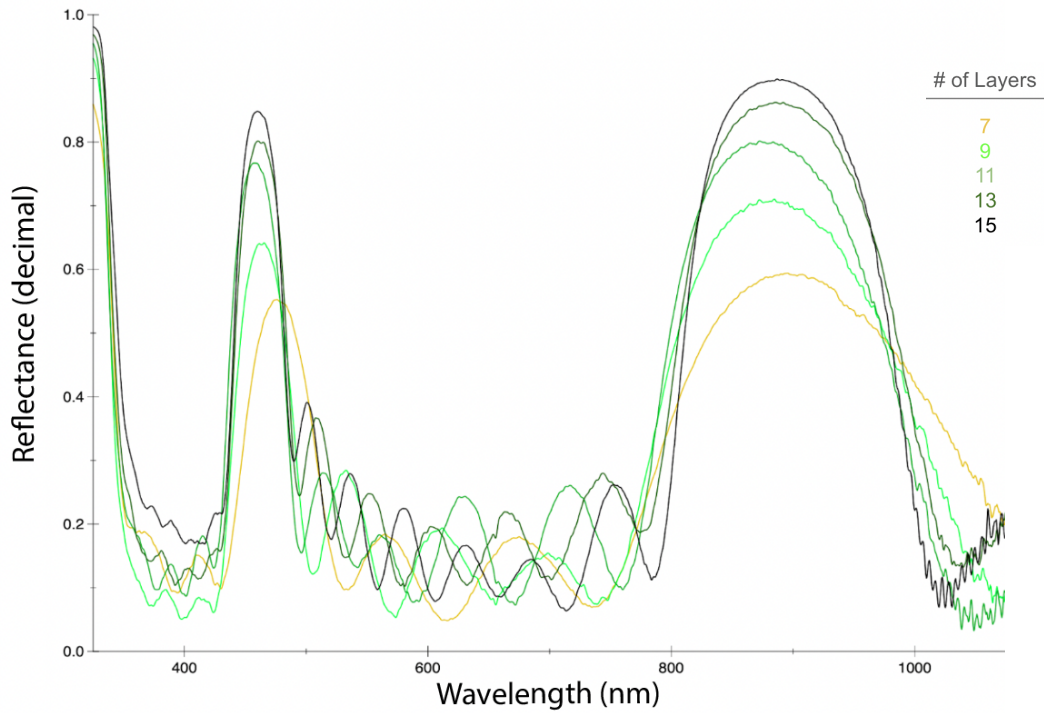
Figure 23: Reflectance spectra progression for DBR-G. Table 6 contains the key data points from these spectra.

The key data points from the DBR-G spectra are contained in Table 6:

Table 6: Key Reflectance Data Points for DBR-G Layering Progression

# of Layers	Peak Location (nm)	Peak Height (%)
7 Layers	889.5	59.4%
9 Layers	878	71.0%
11 Layers	866.5	80.2%
13 Layers	880	86.2%
15 Layers	881	89.9%

In both cases, the approximate 90% reflectance peak height regime is achieved. For sample

DBR-I, only 13 layers were needed to reach a reflectivity peak height of 92.5% at 629.5nm.

Adding the last two layers to retain the constant 15-layer architecture seen in the rest of the eventual continuum boosted this reflectivity to 94.7% at its peak location of 637nm. Each bilayer deposition shows the expected slight-redshifting, peak height increase, and full width at half maximum (FWHM) decrease. DBR-I represents the ideal case, where all expected trends are present and the 90% peak height target is achieved and surpassed. OpenFilters was used to recreate and generate spectra for the 15-layer DBR-I using the AFM thicknesses measurements for its constituent layers, and two different effective titania film RI's for the high RI layers: the constant literature value of 2.12, and the values generated from wavelength-dependent RI function derived in Chapter 2.1.2. These reflectance spectra are presented in Figure 24:
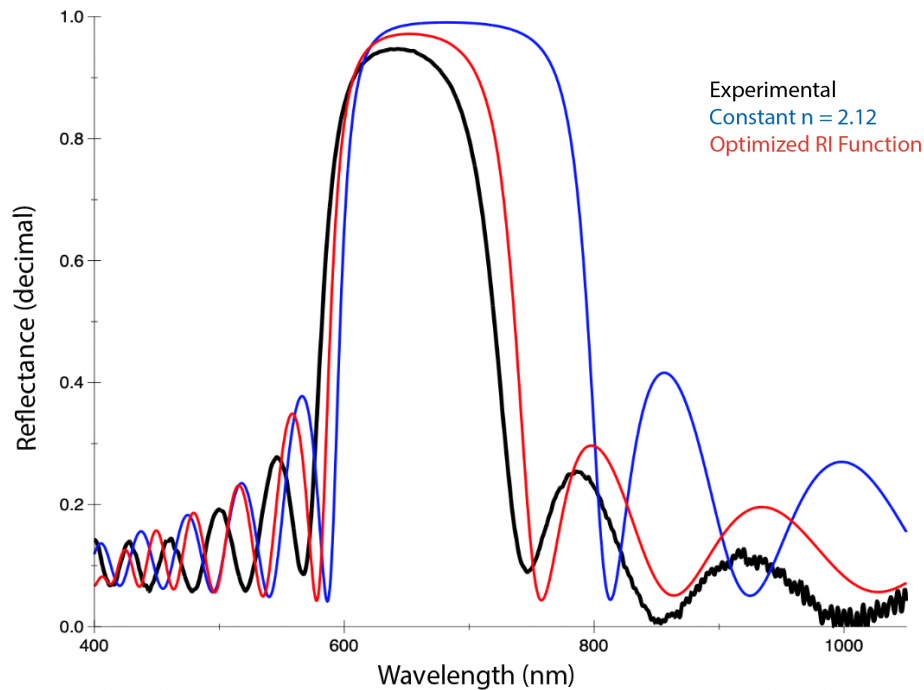
Figure 24: Comparison of DBR-I's empirical reflectance spectra (black), theoretical reflectance spectra using a literature constant of 2.12 for the effective titania film RI (blue), and the theoretical reflectance spectra using the RI function for the titania films derived in this study (red).

This illustrates the need for the optimized effective titania film RI function, and demonstrates its ability to better model this system than the constant literature-provided value. The photonic bandgap is appropriately wide, and the modes before and after it are now better aligned. DBR-G

highlights the preservation of the general overall trends, and reaches the target peak height regime. Despite these accomplishments, the reflectance peak growth progression is provided in Figure 23 to show the degree of error that can arise with solution processing. While each sequential measurement shows a peak height increase and FWHM decrease, there are spectral oddities seen within the 7, 9, and 11-layer progressions. The 7-layer sample is the most red-shifted, which may be attributed to inconsistent depositions producing thicker than average PMMA and titania layers. This could be due to slightly longer than average oven treatments promoting polymer expansion, use of an older and more viscous titania solution, or other user errors. The 9-layer and 11-layer spectra show an apparent blue-shift rather than an expected red-shift when compared to their preceding measurements of 7-layer and 9-layer samples respectively. This is attributed to a number of potential user errors that may have resulted in thinner than desired layers. These include premature precursor deposition on the spinning substrate, failure to fully dispel the more viscous polymer solution in a single pipette evacuation, and off-center deposition of the solutions closer to the edge of the rotating glass. All three errors would result in slightly less solution remaining on the substrate at the end of the 30 second spincoating cycle, thus producing marginally thinner additional layers that would yield the observed blue-shift. Other errors may have arisen during spectrometer setup and calibration. The most probable inconsistency in the measuring process is a slight misalignment of the substrate within the transmission bridge during these two measurements. While utmost caution and precision was used during the measurement process, even a miniscule deviation from normal incidence yields a spectral shift. This is demonstrated in the OpenFilters simulation of DBR-G with slightly varied incident light angles provided in Figure 25:
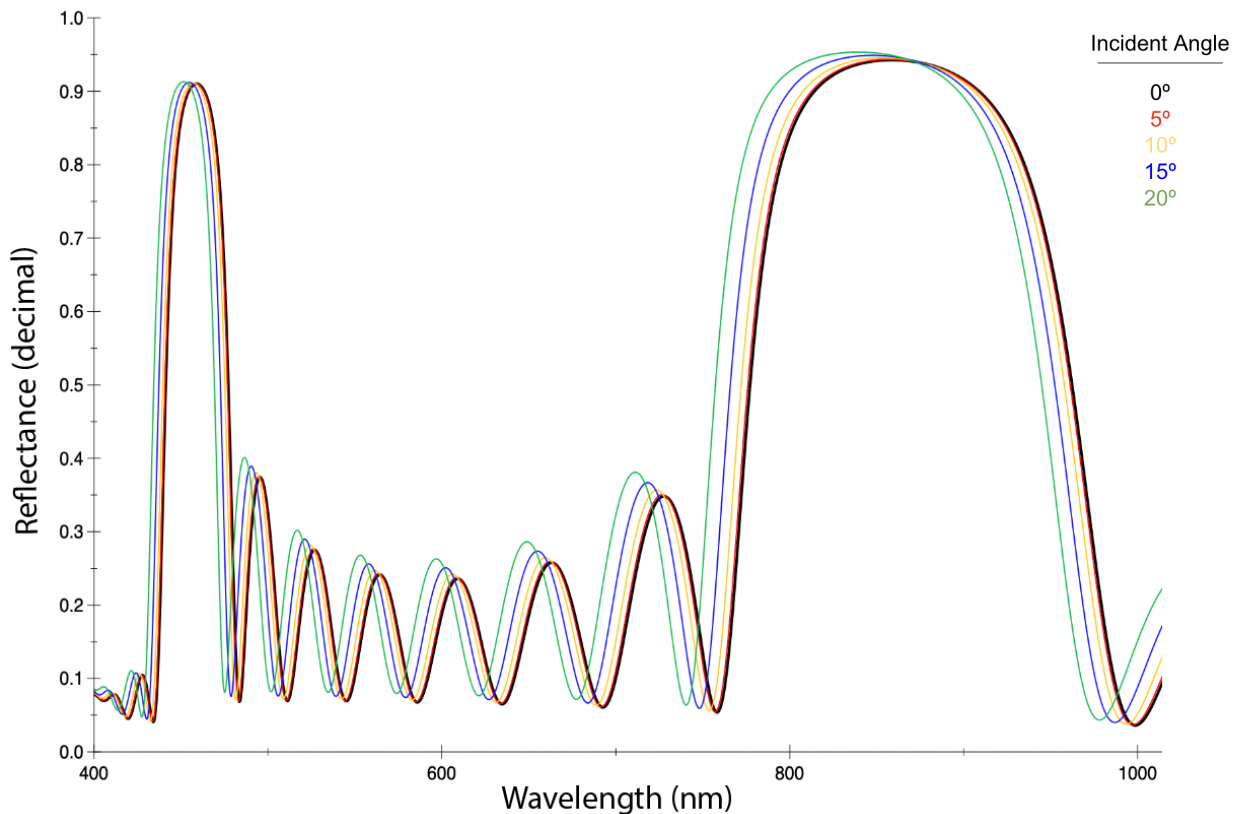
Figure 25: OpenFilters simulations demonstrating slight light incidence angle variation yielding blue-shifted spectra. The bolded black line shows the normal incidence, the red a 5º deviation from normal, while the yellow deviates by 10º, the blue by 15º, and the green by 20º. As the deviation from normal increases the blue-shifting becomes more pronounced.

As demonstrated in the OpenFilters projections, spectral shifting becomes more prominent as light incidence strays from the 0º path that has been designated as normal. This all serves demonstrate that these slight synthetic and characteristic inconsistencies could compound to produce the apparent blue-shifted peaks seen in the 7-layer, 9-layer, and 11-layer spectra for sample G. Despite these oddities, most of the expected trends are seen across the overall progression from a 7-layer to 15-layer DBR. When comparing the 7-layer and 15-layer spectra to one another, the peak FWHM decreases, and peak height increases from 80.2% to 89.9%, however peak location shifts from an unexpected 889nm to 881nm. All expected trends are seen in the progression from an 11-layer to a 15-layer DBR. The FWHM decreases, peak height increases from a considerable 80.2% to 89.9%, while the peak location shifts 866.5nm to

881nm. Despite inconsistencies with this sample, the final product is a solution-processed DBR with and 89.9% reflectance peak height that is attained by deposition of just 15 layers (7.5 bilayers). Moreover, the successful peak height threshold was attained within 15 layers for all samples in the reflectance peak continuum shown in Figure 26:
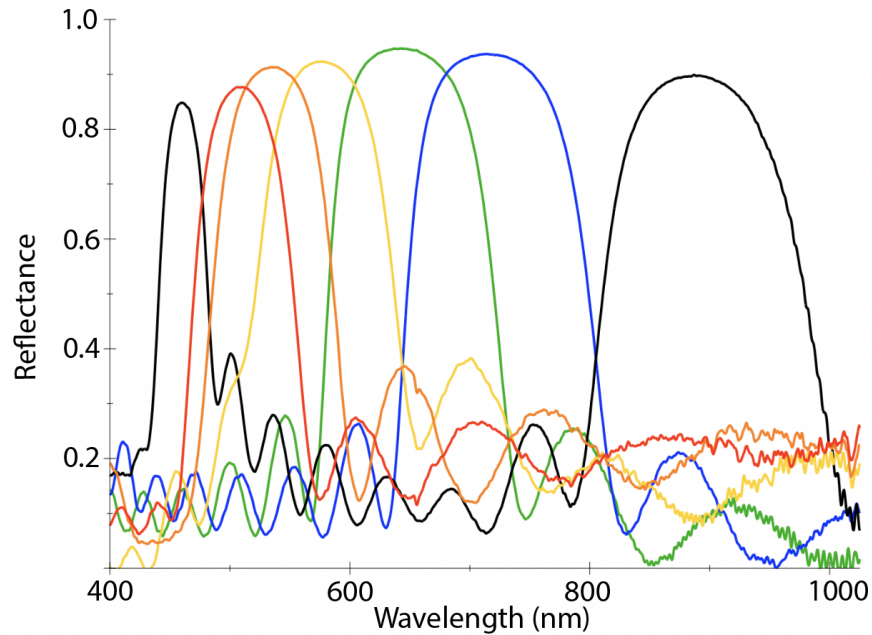
Figure 26: DBR continuum for samples D-I. All photonic crystal stacks are composed of 15 alternating layers of titania sol gel and PMMA films.

This is a notable finding, and further establishes relative ease of fabrication. Note that the continuum graphic does not contain filters DBR-A through DBR-C for the sake of legibility. While they possess the desired photonic bandgap properties, these three filters largely overlap with DBR-F, and only extend the continuum slightly further into the lower wavelength regime. All 9 Filters are shown in Figure 27:
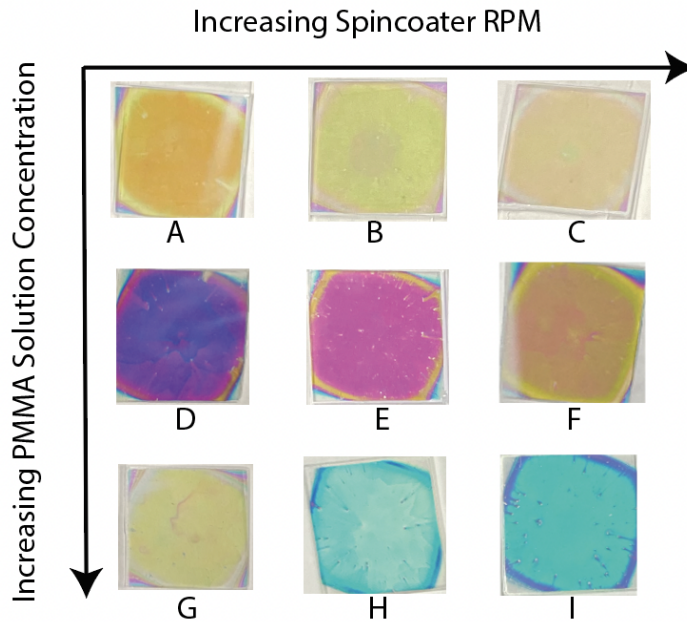
Figure 27: Images taken of the 15-layer DBR stacks

These solution-processed, colorful filters show satisfactory uniformity and are structurally sound. While some more difficult to process high-RI-inorganic:low-RI-inorganic DBR's have achieved these 90% heights in as few as 7 layers, other easier to fabricate low-RI-organic-polymer:high-RI-organic-polymer systems have required anywhere upwards of 20 layers and as high as 128 layers for the same result [8] [22] [27]. The inorganic-inorganic DBR challenges can be attributed to difficulties in evenly distributing the often-used colloidal SiO_2 spheres as the low RI material, which is an extensive field of study in its own right [28][29]. The synthetically facile high-RI-inorganic:low-RI-organic-polymer structure allows for sufficiently high near-90% reflectivity peaks to be reached in relatively few bilayer depositions, namely 7.5 in this case, which is in accordance with papers that have used other organic and inorganic materials that possess larger RI contrast and have achieved these feats with 4 bilayers [26]. A literature study that uses colloidal TiO_2 and PMMA as their solution-processed layering materials utilizes a considerably more complicated titania nanoparticle workup that relies on

vacuum processing, and requires between 12 and 18 bilayers to achieve near-90% reflectance peak heights [30]. This study demonstrates three reflection peaks ranging from 453nm to 619nm [30]. Another study's continuum with the same TiO_2:PMMA architecture spans a larger range, but with heights on the order of 60% [31]. The presented thesis' results extend the first studies continuum range from 487nm to 881nm with room for expansion in either direction, and maintain 90% peak heights. The additional 228nm of control coupled with the need for fewer bilayer depositions facilitates the opportunity for easier incorporation and use as waveguides in multijunction, LSC-equipped solar cells. The peak continuum location expansion allows for more DBR - PLNC - semiconductor combinations, while the fewer number of bilayers produces a thinner overall stack, which facilitates easier embedment in real devices.

3.2 Cesium Lead Halide Perovskite Microcavity Development

Photoluminescent nanocrystals play a critical role in all outlined applications. Of particular interest to the presented study and its future directions is discovering how to embed them between DBR mirrors to form an LSC environment. All work to date has focused on the synthesis and processing of Cesium Lead Halide ($CsPbX_3$) nanocrystals. Thus, it is important to further detail how they are produced in lab and what attempts have been made to create these structures.

3.2.1 Perovskite Synthesis

Traditional perovskite nanocrystal syntheses often require air-free environments and high-temperature conditions. To align with a key principle of the DBR project at hand, namely ease of fabrication, these challenging requirements are circumvented by employing a modified version of the $CsPbBr_3$ synthetic protocol detailed by Brown et al. They have formulated an innovative, air-free, room-temperature reaction schema that yields $CsPbBr_3$ PLNCs with high photoluminescence quantum yield, uniform size, and sufficient stability [12]. Three precursor solutions are created in the reaction scheme's workup. First, cesium carbonate (Cs_2CO_3) is

dissolved in octanoic acid. This gives a solution containing cesium octanoate and excess octanoic acid [12]. Next, Lead bromide ($PbBr_2$) is dissolved in toluene through the addition of trioctylphosphine oxide (TOPO). This solution stirs at 80ºC for roughly 30 minutes, or until all constituents are completely dissolved [11]. These two solutions provide the reactants that will produce the perovskites when introduced to one another. Finally, a didodecyldimethylammonium bromide (DDAB) precursor is created. This is done by adding DDAB to toluene, and vortexing until the solution is clear [12]. This solution is used to quench the reaction, and provide DDAB capping ligands that ensure size uniformity of the crystals.

The reaction procedure is simple and takes place in a well-stirred three-prong vial. First, 2mL of $PbBr_2$ precursor solution is added to the vial. Under strong stirring 220uL of the cesium octanoate solution is added to the vial as well, beginning the nucleation and growth phase of the perovskite synthesis. The solution then turns a bright yellow-green color indicating the precipitation of the $CsPbBr_3$ PLNCs. After 5 minutes, 624uL of the DDAB solution is added under strong stirring to quench the reaction. The vial is allowed to stir for 5 minutes longer, providing sufficient time for the DDAB ligands to stabilize the nanocrystals. The DDAB ligands also increase yield and limit nanocube growth such that the product diameter is held between 8 and 10nm. The reaction scheme is detailed pictorially in Figure 28:
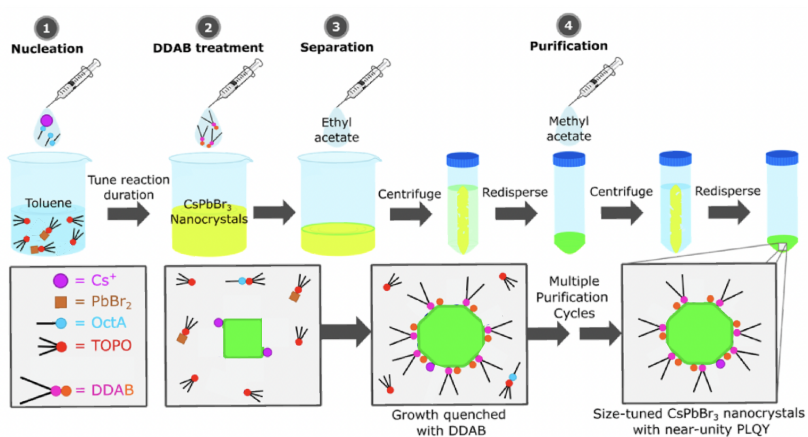
Figure 28: $CsPbBr_3$ Perovskite reaction scheme [12]

3.2.2 Perovskite Characterization

High photoluminescent quantum yield, broad absorption regimes, and narrow emission bands are characteristic properties of cesium lead halide perovskites that make them ideal for use in optoelectronic applications. These are quantified with typical spectroscopy measurements using a StellarNet BLACK-Comet C-SR-50 Spectrometer. The emission band is analyzed via photoluminescence (PL) spectra. This measurement is taken by diluting 200uL (or roughly 12.5%) of product stock solution in 4mL of toluene in a glass cuvette. The cuvette is then placed in the appropriate holder, which is fitted with a fiber optic cable that connects the spectrometer. A 395nm UV flashlight is used as the photoexcitation source, and is held roughly 3 inches away from the cuvette. The absorbance spectra is measured using the same setup, however a StellarNet SL5 Deuterium + Halogen light source is used instead of the UV flashlight, as it provides a broad set of incident light wavelengths. A typical absorbance and normalized PL spectra are provided in Figure 29:
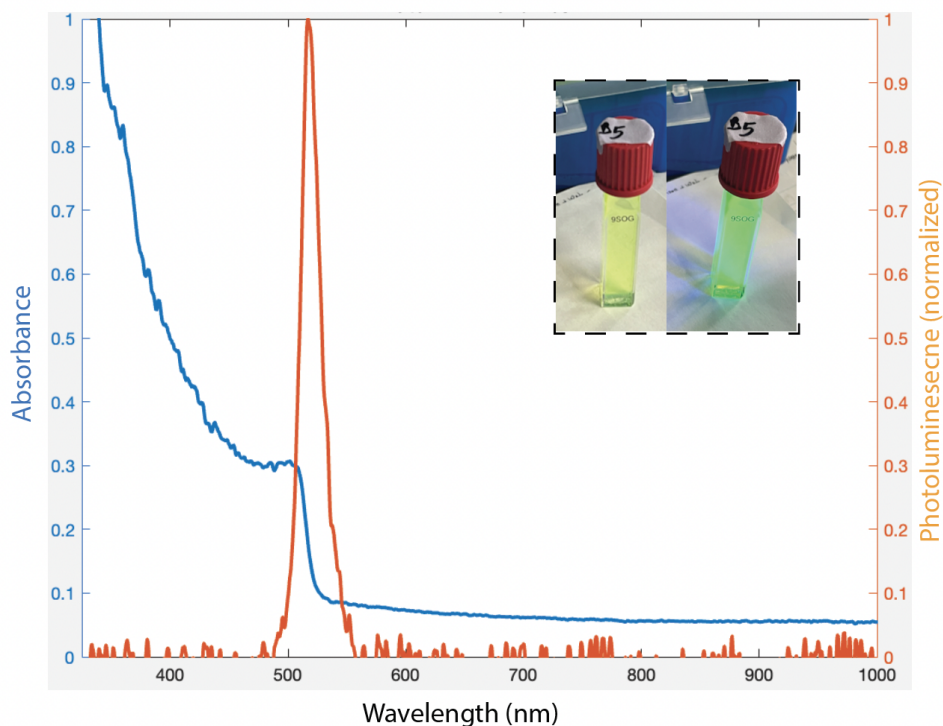
Figure 29: Experimental absorbance (blue) and PL spectra (orange) for CsPbBr$_3$ perovskite nanocrystals. The inset shows images of the samples under room lighting (left) and UV excitation (right).

All expected trends in both plots are present. First, the absorbance spectrum shows very large, near-unity absorbance values that fall with increasing wavelength. When the absorbance spectra intersects the lower bound of the PL emission band, it drops severely before plateauing toward zero as expected. This is known as an absorbance shoulder. The PL curve shows a narrow, normally distributed emission band centered about a 517nm peak. These spectra show the desired high absorbance at low wavelengths, appropriate shouldering trends, and expected resulting Stoke's shift in the PL peak location. The 517nm peak falls within the desired range for green CsPbBr$_3$ nanocubes, and indicates a successful synthesis. Note that throughout this study, the peak has seen location values vary slightly due to inconsistencies in the synthesis. These include precursor concentration inconsistencies, precursor degradation with time, and irregularity (on the order of seconds) of quenching DDAB injection during synthesis. Despite this error margin, all emission wavelengths are within the green wavelength regime.

3.2.3 Microcavity Synthesis and Results

Optical cavities are present in both LSC and lasing applications. In both environments, the cavity refers to a layer that breaks the one-dimensional symmetry of the device in question [4]. This layer is usually deposited in the central layer of the stack. In lasers, the optical cavity refers to the gain medium regime that is surrounded by mirrors on either side. In LSC environments the optical cavity plays an analogous role, often placing emissive materials between two reflective mirrors. For the purposes of this study, the microcavity layer refers to the $CsPbBr_3$ perovskite-containing layer that is to be placed between two, equivalent DBR mirrors that reflect light at wavelengths overlapping with the emission peak of the perovskites in question. To first mimic the microcavity on its own, rather than sandwiched between completed DBR crystals, the microcavity environment is recreated and examined by depositing perovskites between two titania films: their effective local environment in a given DBR-LSC device. It is well known that nanocrystal stability and fluorescence depends largely on the local chemical environment [17] [18]. As such, embedding the cavity into DBR stacks proved to be difficult, as perovskite photoluminescence significantly diminished when trying to stabilize them between the two layers of titania. The titania layers and the perovskites they encompass are regarded as the microcavity in these experiments. Again, all layer depositions were completed through a solution-processed spincoating procedure much like all others in this study. To embed the unstable nanocrystals in a host polymer matrix, $CsPbBr_3$ product stock solution with one part 40 $\frac{mg}{mL}$ polystyrene (PS) in toluene solution to create a 50% quantum dot solution by volume. 200uL of this solution was dropped at 2000 RPM in a given sample to produce the perovskite-embedded microcavity layer. The original stock solution and 1:1 stock:polystyrene solutions are shown in Figure 30 under both room lighting and UV flashlight excitation:
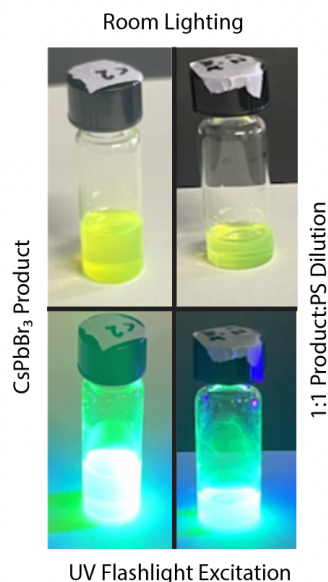
Figure 30: Grid showing preservation of CsPbBr$_3$ perovskite photoluminescence when reaction stock is combined in a 1:1 volume ratio with a PS in toluene solution. Both solutions are shown under room lighting and UV flashlight excitation.

It is clear that the nanocrystals are still highly photoluminescent when mixed with the PS solution. This mixture was made to provide a polymer matrix within which the perovskites could be evenly distributed and reside after solvent evaporation during spincoating. This provided minimal stability, with only few perovskites surviving both titania depositions and oven treatments. This was improved by depositing a sacrificial layer of PS on the initial titania layer to improve distribution, and then depositing another layer of protective PS on top of the PS-Perovskite matrix. This spincoating progression provides an interstitial layer of PS between the perovskite:polymer matrix and the surrounding two titania layers. This was done after numerous lab trials revealed that direct titania:perovskite contacting yielded interactions that degraded the nanocrystals and extinguished their photoluminescence. These stability improvements were visualized using a VWR UV Transilluminator, and are depicted in Figure 31:
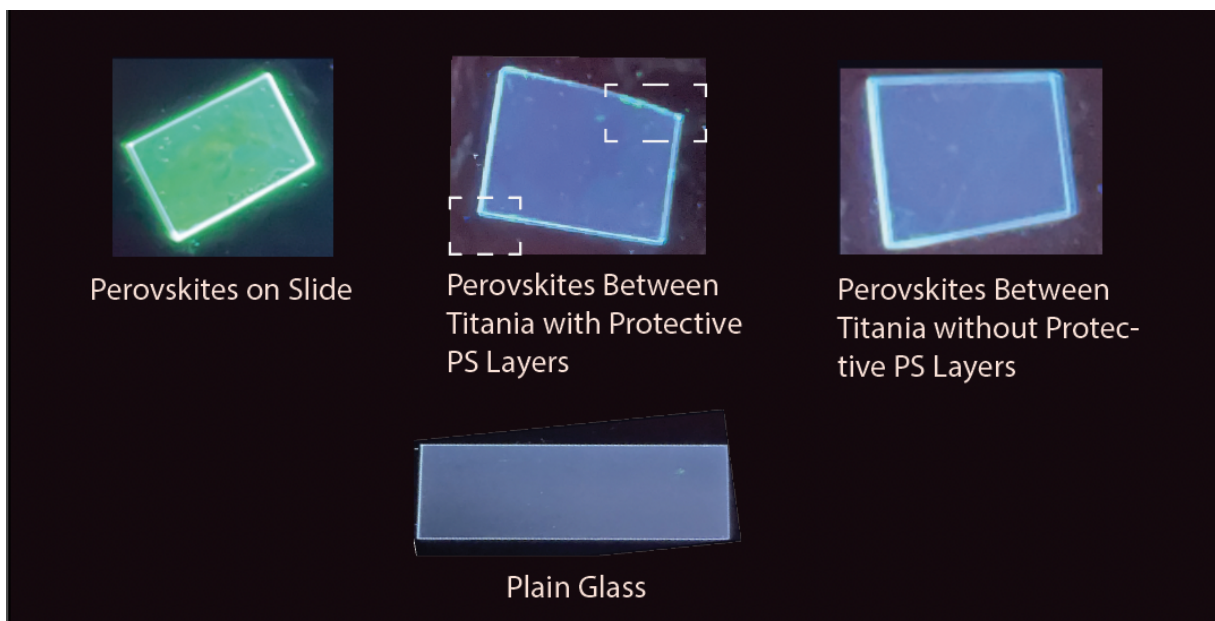
Figure 31: Transilluminator-excited Perovskite Films and Microcavities. White dotted boxes highlight the few green-emitted perovskites that were successfully protected from the titania sol gels with an interfacing PS film.

While the perovskites deposited on a thin sacrificial PS polymer layer with no other neighboring films are still very photoluminescent, it is clear that encapsulation between titania films extinguishes any visible re-emission completely. While the protective polymer sample still sees degradation of the majority of the perovskites, some of these nanocrystals in the corners of the microcavity structure were able to survive the titania film encapsulation, and are still emitting green light. A StellarNet IS6 integrating sphere setup was used to measure the emission spectra of these three samples. The integrating sphere was selected over the previous spectrometry setup as it allows for capture of all emitted photons due to its perfectly reflective interior, and spherical geometry. These parameters ensure that all output photons will be incident upon the photodetector. The light source for this experiment was a Pico G2V Solar Simulator, which was fit squarely into the input port of the integrating sphere. The simulator's 398-412 LED was used to excite the film samples and collect the spectra shown in Figure 32:
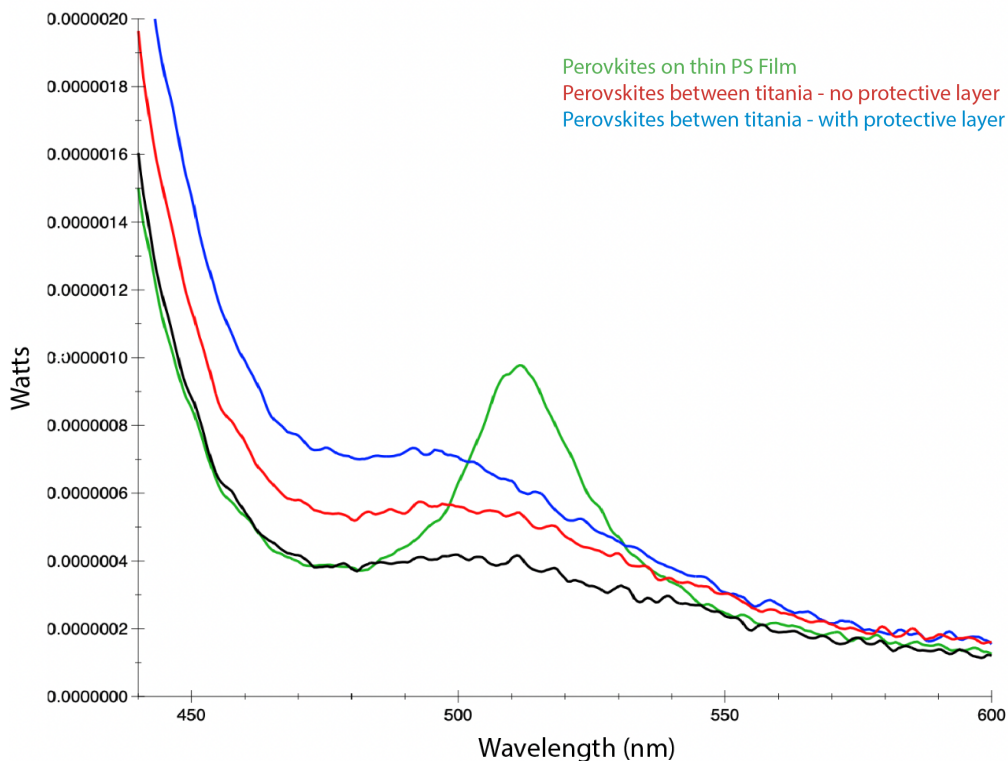
Figure 32: An up-close look at the expected emission peak domain for the perovskite film in the absence of titania encapsulation (green), placed directly between two titania films (red), with a protective PS layer to prevent contact with the surrounding titania (blue), and the control plain glass slide spectra (black).

Figure 32 provides emission spectra for the samples shown in Figure 31. The large slope at lower wavelengths that lead into the emission peak regime corresponds to the LED light source. Clearly, the highly photoluminescent nanocrystal film retains a well-defined emission peak in the absence of any titania in its local environment. When placed directly between two titania films, significant amounts of photoluminescence is lost, as the spectra more closely matches that of a plain glass slide with no discernable emission peak. Instead a very broad emission regime emerges.The spectra for the perovskite film sheltered from direct titania contact by a PS protective layer does not retain a well-defined peak either, but it is clearer than that of the non-protected case and shows broad emission of greater area. At all points, this curve is taller than its non-protected counterpart, corresponding to a larger perovskite preservation. The shift

in emission location is expected as it is highly dependent on the local environment [15] [18]. This demonstrates that a more stable perovskite environment has been created, making tangible progress toward a microcavity that is able to be sandwiched between two 15-layer DBR structures, and form a LSC device. The future work of this project will largely focus on further stabilizing this microcavity's perovskite layer and quantifying its photonic efficiencies.

Chapter 4: Future Work

The primary goal of this work has been attained: creation of a fully solution-processed photonic crystal system, with reflectance peaks that span the visible spectrum continuum and have peak heights on the order of 85-90%. These DBR stacks possess properties that make them suitable to act as waveguides in LSC and lasing applications. Work that expands beyond the scope of this DBR project has already taken place, as seen in the $CsPbBr_3$ syntheses and preliminary LSC microcavity environment data. Future steps for this ongoing microcavity stability study, DBR continuum improvements (with preliminary data), and desired eventual LSC continuum are detailed further.

4.1 Improving Refractive Index Contrast in DBR Crystals

Through increasing the refractive index contrast between the high RI and low RI layering materials, the functionality and ease of fabrication of the DBR mirrors can be improved. Taller, more defined reflectance peaks form in fewer layers as this contrast is further enhanced. Thus, by increasing this contrast, the desired 85-90% reflectance peak heights can be achieved in fewer than the presented 15 layers. Conversely, a larger RI differential would yield a 15-layer material with taller reflectance peaks approaching unity. The ideal outcome of these future works is to achieve photonic bandgaps with near-unity reflectance peak heights in as few layers as possible. This will give the optimal device performance with the easiest realizable fabrication protocol.

4.1.1 Colloidal Silica as the Low Refractive Index Material

The first strategy for increasing the RI contrast between the two materials is to reduce that of the low RI constituent. The current low RI material in the DBR system, PMMA, is again cited as having an RI of 1.5 in low wavelength regimes, which gradually falls to 1.45 as wavelength increases from 300nm to 1700nm [32]. While this organic polymer has yielded the desired results for the purposes of this work, there are inorganic materials which are cited as both having considerably lower refractive indices as well as being compatible with an entirely solution-processed DBR system. Of particular interest is silica (SiO_2). Silica is cited as having an RI that ranges between 1.23-1.25 [8]. Anaya et al. has produced a solution-processed DBR system that employs the same titania sol gel used in this thesis as the high RI material, but instead uses colloidal silica spheres as the low RI constituent. Their work has approximated the RI of this colloidal silica layer in this system as 1.29 in the 400-800nm domain [8]. They were able to produce a sufficiently tall reflectance peak continuum in just 7 layers, although their continuum spans a smaller, more blue-shifted range [8]. The 85-90% peak height attainment in just 7 layers exemplifies the efficacy of using the SiO_2 with RI 1.29 as the low RI material, as compared to this study's use of PMMA with an RI of about 1.5 and requiring 15 layers to achieve the same effect. As such, future work for this DBR study includes replacing PMMA with silica to achieve desired performance in fewer layers, while expanding upon the continuum provided by Anaya et al. in the deep-red and IR regime. Initial experiments have already been conducted, and preliminary results have been collected. These stacks are constructed using the same titania high RI layer deposition parameters, while the low RI silica layers require a more intricate synthesis. First, 150uL of a 1-4 wt% colloidal silica in ethanol solution is spun between 3000-5000 RPM for 30 seconds. Next, a 0.5 wt% PS layer is deposited directly on top of the silica. This is done to overcome the spherical geometry of the silica particles, as the polymer deposition serves to contain the spheres in a porous matrix structure. The high RI, oven

treatment, low RI cycle is repeated until the desired number of layers are deposited. The

preliminary reflectance spectra are shown in Figure 33:
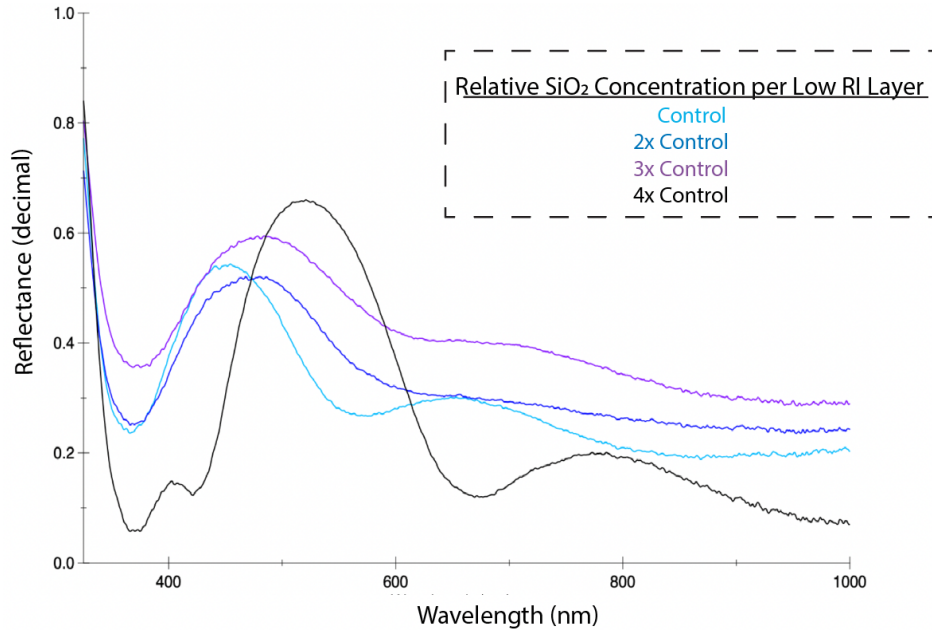
Figure 33: Reflectance spectra for 7-Layer DBRs with varying SiO_2 concentration
in each low RI layer. Each curve color indicates a multiple concentration articulated
in the inset. Images of these structures are shown in Figure 34.

At present, this system has experienced a high degree of structural instability attributed to the

low RI layer. The spectra show very little reflectance peak tunability and the photonic bandgaps

are broad, poorly defined, and have peak maximums on the order of 50-60%. The lack of

tunability is likely attributed to the polymer matrix deposition on top of the silica. The supporting

presumption is that this matrix fixes the low RI layer thickness in every case, and the

polystyrene RI dominates that of the silica. The broad, poorly defined peaks are attributed to

structural instability brought about by the colloidal silica spheres. The homogeneity of these

stacks decreases significantly with each alternative layering and oven treatment, as seen in

Figure 34:
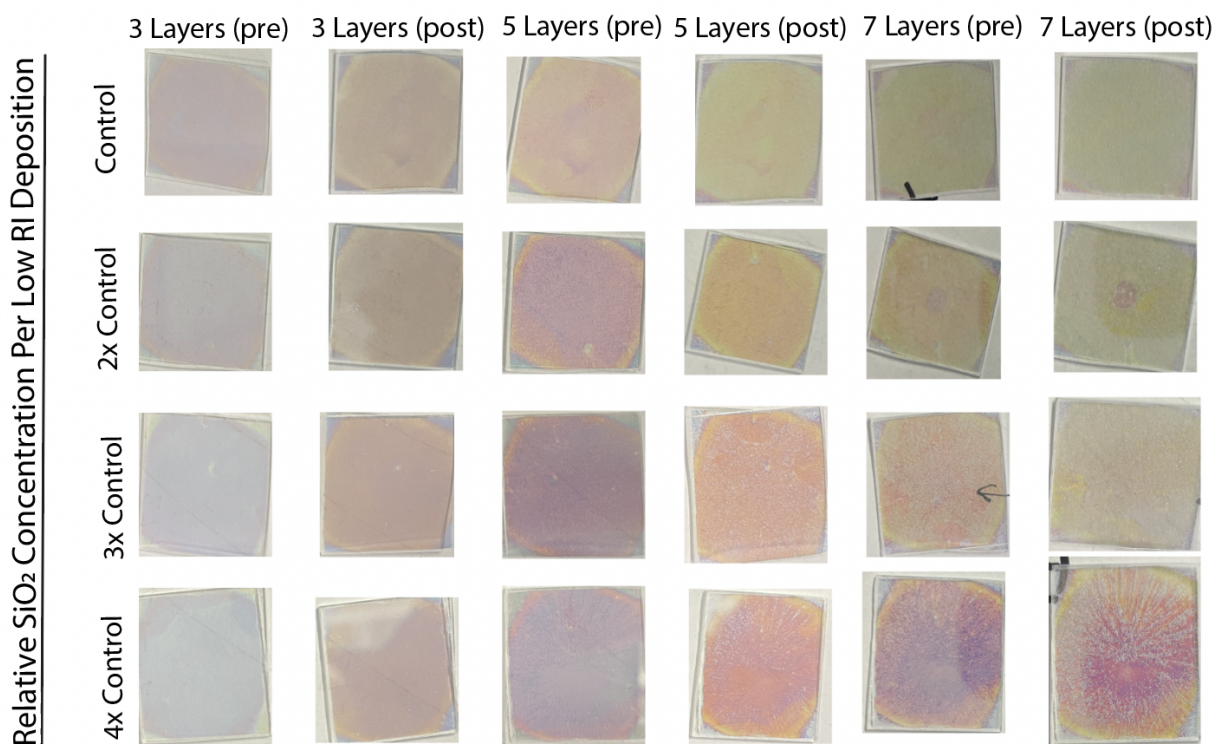
Figure 34: TiO$_2$/SiO$_2$ DBR mirror progression. SiO$_2$ low RI layer concentration increases from the top to bottom row. Pre and Post labels refer to images taken before and after oven treatment respectively.

While the TiO$_2$/PMMA stacks are highly uniform and saturated with vibrant color, these TiO$_2$/SiO$_2$ stacks develop silica aggregations that become increasingly disruptive with each bilayer addition. When the final 7-layer environment is complete, the colloidal aggregates have effectively disrupted the entire film, and the DBRs are almost entirely colorless in most cases. These aggregates and structural collapse are thus thought to be culpable for the poor reflectivity observed in these structures. To improve this, a number of new synthetic strategies have been formulated. First, the single, large silica solution deposition will be replaced with several, high RPM depositions for a single low RI layer. This will ideally facilitate a more uniform distribution of spheres across the glass substrate, and avoid the "spider web-like" pattern that develops in the current structures. Next, silica solution concentration will be expanded beyond the 1-4 mol%

regime, and coupled with this new deposition technique again with the intent to create a more uniform low RI layer. Finally, in accordance with Anaya et al., future studies will utilize a 400ºC heating treatment rather than the usual 75ºC oven treatment used in the preliminary trials. In theory, this will better anneal the titania into a more dense film, providing a higher RI while also melting out the PS matrix and leaving behind only the colloidal silica sphere network. In this way, it is believed that the PS will no longer dominate the lower RI layers, allowing the lower RI silica network RI to couple with the even larger RI titania films to produce stronger, more tunable reflectance peaks. When structural stability is achieved, DBR stacks with varying low RI layer thicknesses and concentrations will be produced in an attempt to achieve the same degree of tunability seen in the presented study.

4.1.2 Addition of Titania Nanopowder to the High Refractive Index Titania Film Solutions

Just as decreasing the refractive index of the low RI material in a DBR stack can widen the RI differential between the two layering constituents, increasing the RI of the high refractive index material can impart the same effect. Again, by expanding this contrast disparity the ease of fabrication can be improved by yielding taller, sharper peaks in fewer necessary layer depositions. Literature has indicated that titania nanoparticles have an exceptionally large refractive index, reaching as high as 2.7 at 500nm [33]. Analogous to the use of colloidal silica as the low RI layering material, future research will focus on the incorporation of commercially produced titania nanopowder in the high RI layers. The first set of tests will focus on the addition of this powder to the current TTIP solutions used to produce titania sol gel films. The rationale behind this experimentation is an expected increase in titania film effective refractive index due to the inclusion of these nanoparticles. Ideally, the nanoparticles will be soluble in the TTIP solutions, dissolve into the existing sol gel while retaining a high RI properties, and eventually create a larger "average" titania film refractive index. It is likely that the nanoparticles will require a more complicated workup to be soluble in this way, and thus the second set of testing

will focus on titania nanoparticle solubility optimization in the current sol gels, various solvents, and across a number of concentrations. Once a workup that facilitates the the formation of a successful TTIP sol gel and titania nanoparticle hybrid solution is determined, the effective RI will be determined through the same measures used in this study prior: single film reflectance measurements coupled with OpenFilters projections in a chi square testing sequence. When it is confirmed that a larger RI film has been developed, new DBR stacks will be created using these films to test stability and functionality.

4.2 Enhancing Stability of the Green $CsPbBr_3$ Perovskite Microcavity

Perovskite stability itself is an expansive field of study, as these materials are known to be highly degradable. The preliminary data shown in Chapter 3.2 leads into the key next steps in this study. As seen in figure 33, deposition of nanocrystals on top of a thin sacrificial PS layer provides a clear perovskite emission peak, while surrounding this emissive layer with titania films completely extinguished their photoluminescence. Recall that the surrounding titania films mimic the local environment the perovskites would experience in an LSC system, in which two DBRs would have an emissive perovskite layer sandwiched between them. To mitigate this emission loss, the protective PS layer interfaces between the perovskites and the top titania layer in an attempt to preserve the PLNCs. This brought about slight improvements: namely the presence of a broad, blue-shifted emission band. Although this emission band is poorly defined and still shows notable perovskite emission loss, its presence suggests that the PLNCs are better-preserved with the interfacing polymer than without. It is a paramount, near-future goal of this study to continue investigating the efficacy of protective layers in this application. Immediate steps include examining other polymer species (beyond PS and PMMA), varying polymer solution concentrations, and optimizing spin coating deposition parameters. Near-future steps also include exploration of the DDAB capping ligand exchange that has provided sufficient perovskite endurance thus far, utilization of a Schlenk line for air-free perovskite syntheses, and

development of $CsPbBr_{3/}SiO_2$ core/shell nanocrystal syntheses. When clearly defined emission

peaks emerge in the mircocavities , focus will shift on then optimizing the photoluminescent

quantum yield (PLQY) of these emissive microcavity environments. PLQY is the key metric of

interest for these perovskite cavities, and is defined as the number of incident photons absorbed

by a PLNC divided by the number of photons emitted:

$$PLQY \ = \ \frac{number\ of\ absorbed\ photons}{number\ of\ emitted\ photons} \times 100\%$$

Although cesium Lead Halide perovskites in solution are noted for their near unity PLQY, they

were observed to be considerably less efficient in the current microcavity configurations [12].

Following the emergence of narrow band emission peaks from titania-contained,

polymer-protected, $CsPbBr_3$ perovskite-laden microcavities that have high PLQY, focus will shift

to the formation of an entirely solution-processed LSC environment discussed further in Chapter

4.3.

4.3 Developing the Green $CsPbBr_3$ Perovskite Microcavity / Green DBR LSC System

Embedding a green-emitting $CsPbBr_3$ perovskite microcavity between green reflecting DBR

stacks creates an LSC environment that allows for photon trapping, concentration, and direction

towards a semiconductor in a real solar module. This is shown in Figure 5, which shows the

reshaped emission. At present, highly reflective green wavelength DBRs and green-emitting

perovskites have been successfully synthesized, and their respective reflectance and

photoluminescence peak overlaps are shown in Figure 35:
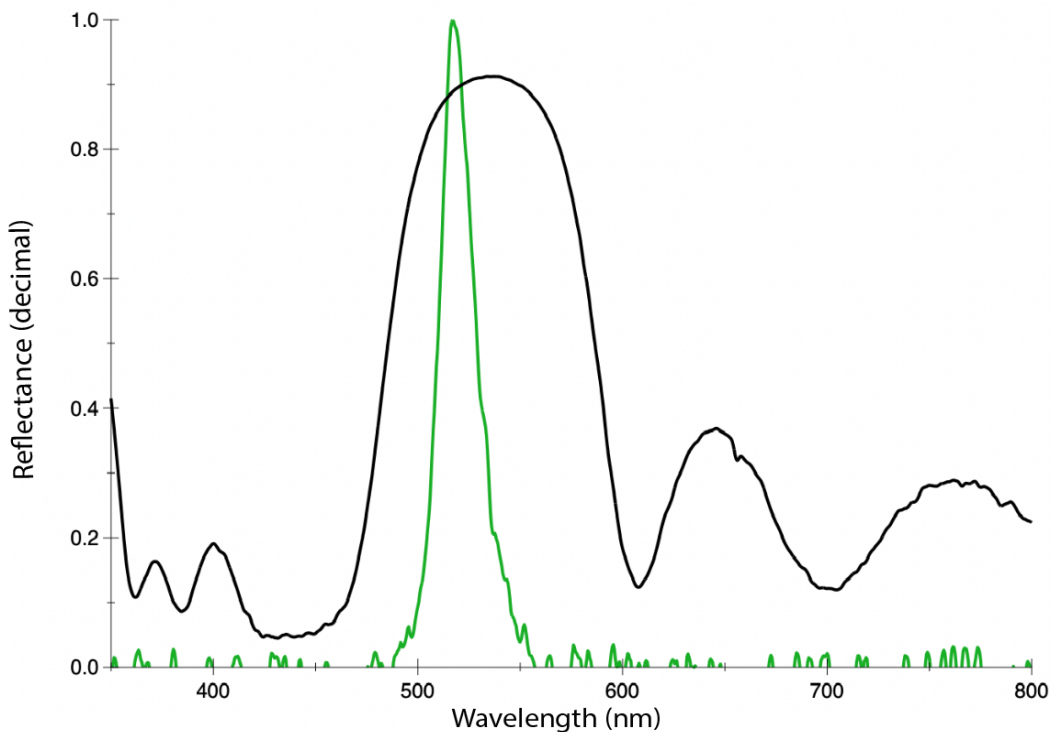
Figure 35: Overlapping reflectance spectra from DBR-E (black) and PL emission peak from the perovskites measured in Figure 29 (green).

This overlap, coupled with the preliminary emissive microcavity stability improvements, demonstrate that the formation of this LSC environment is theoretically feasible at present. The emission peak is contained entirely within the DBR's photonic bandgap, allowing for light trapping via TIR. These architectures will be pursued upon the development of a microcavity with sufficient PLQY. The LSC design is completely solution-processed as well. Initial trials will consist of creating a 15-layer, green-reflecting DBR via the usual spin coating protocol, depositing the optimal emissive microcavity on top of this mirror, and then spin coating a second DBR mirror on top of the cavity. In the event stability failures arise, appropriate tests analogous to those detailed in Chapter 4.2 will be conducted.

4.4 Exploring Emitters and LSCs in Other Wavelength Regimes

The ultimate vision for this project is to take the findings of this study, namely the DBR reflectance peak continuum, and translate it into an LSC continuum. Once the quantities for the current green LSC design of focus reach desired thresholds for real solar cell module use, focus will shift to synthesis of nanocrystals that re-emit in other wavelength regimes, with particular interest in the IR regime. Each emitter will then undergo trials to develop functional microcavity environments for all species. The LSC continuum will be fleshed out by embedding these photoluminescent cavities into appropriate DBR stacks, namely those with reflectance bands that overlap with their emission bands. It is in this way that the produced DBR continuum offers powerful waveguiding capabilities across the visible spectrum and beyond for next-generation solar applications: they can be paired with emitters and semiconductors whose emission energies and bandgap energies respectively overlap with the photonic bandgap of a given DBR. An LSC continuum facilitates the formation of high efficiency, multijunction solar cell design as seen in Figure 36:
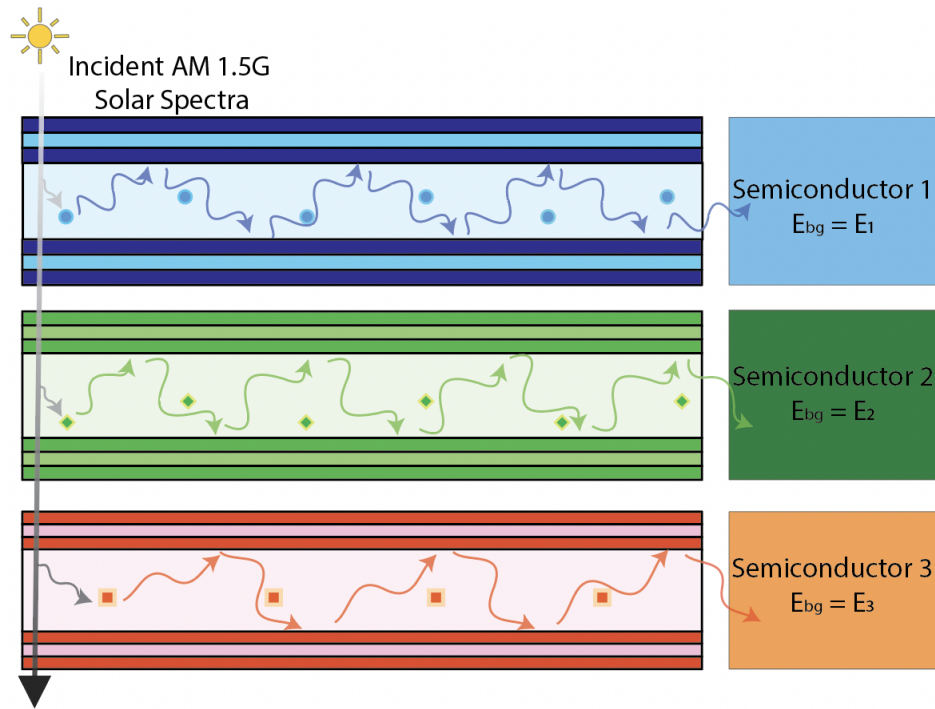
Figure 36: Demonstration of A.) isotropic PLNC emission B.) incorporation of PLNCs into a DBR stack to reshape emission and C.) pairing PLNCs with DBR stacks that reflect at their emission wavelength, converting broadband sunlight into photons with characteristic wavelengths that match semiconductor bandgap energies in a multijunction solar cell.

Multijunction modules have theoretical efficiencies on the order of 50% and higher, significantly pushing the thermodynamically determined Shockley-Queisser Limit of 30% for a standard, single junction silicon cell [34]. In this way, the DBR continuum's translation into an LSC continuum, and eventual design of multijunction cells will allow for development of high efficiency, next-generation solar devices that will facilitate the necessary deviation from fossil fuels, and standardization of renewable energy practices

Chapter 5: Conclusion

This work sought to design and fabricate an entirely solution-processed Distributed Bragg Reflector system, whose reflectance peak continuum spanned the order of hundreds of nanometers and retained maximum values on the order of 85-90%. A high RI titania sol gel film was selected as the first layering material, and a low RI PMMA constituent was chosen to be the second. It was determined through atomic force microscopy that thicknesses of these layers could be controlled through varying the concentration of the precursor solutions, and the spincoating deposition RPM. These measurements revealed consistency for each set of RPM and concentration combinations in both species, and verified that they were on the order of nanometers thick. The titania films were deposited in 200uL quantities at 2000 RPM in all cases. The less concentrated TTIP1 titania precursor solution returned average film thicknesses of 61.22 ± 3.63 nm, while the more concentrated TTIP2 precursor yielded an average thickness of 84.67 ± 5.42 nm. Due to sol gel films having unique optical properties that differ from their idealized nanoparticle counterparts, a chi-squared fit test was conducted to find the effective RI of these films as a function of wavelength. This was achieved by using the AFM-determined thicknesses to fit theoretical TMM plots for constant RI values to the experimental reflectance spectra, and then finding X^2_{min} for 25nm intervals in the 400-625nm domain. The MATLAB curve fitting toolbox then optimized a polynomial expression to model results, and returned a function that better modeled the effective RI of these titania films as evidenced by better fitting of both single film and completed DBR reflectance. PMMA films were deposited in constant 150uL amounts for three different concentrations at spincoating speeds that varied between 2000-6000 RPM. The least concentrated polymer solution of $10.03\frac{mg}{mL}$ spun at 6000 RPM gave the thinnest polymer film measured as 34.10 ± 2.59 nm. Conversely, the $40.12\frac{mg}{mL}$ PMMA solution spun at 2000 RPM gave the thickest polymer film of 180.09 ± 7.30 nm. AFM measurements assert that

increasing precursor solution concentration will yield thicker layers, while spincoating RPM increases yield thinner films.

Through alternative spincoating of these films, it was determined that 15-layer DBRs composed of varying PMMA layer thicknesses could produce a sufficiently tall reflectance peak continuum that spans 400nm of the visible spectrum. These waveguides are on the order of microns thick, as confirmed by AFM, and have reflectance properties that make them suitable for use in LED, LSC, and lasing applications. With this success, preliminary experimentation on a solution-processed perovskite-containing microcavity to be embedded between two identical and appropriate DBR stacks, thus creating an LSC environment, was conducted. $CsPbBr_3$ perovskites were synthesized via an in-air protocol, and were determined to have the desired narrow green emission band and expected shouldering absorbance characteristics. UV-transillumination visual cues coupled with photoluminescence measurements conducted in an integrating sphere demonstrated a near-complete loss of perovskite emission when placed between titania films. Polystyrene protective films used to prevent direct contact between the perovskites and the titania demonstrated an incremental increase in nanocrystal stability, and yielded a broader, blue-shifted emission peak. Immediate future work will continue to optimize the stability of the perovskites in this cavity while simultaneously looking to increase the refractive index contrast between the high RI and low RI layers used in the perovskite-free DBR mirror continuum. Subsequent long-term project goals include successful fabrication of a complete green-wavelength LSC, and exploration into luminescent nanomaterials that emit in other wavelength regimes with the ultimate goal of translating the present DBR continuum into an LSC continuum. In this way the solution-processed systems that constitute this project and its future directions align with global sustainability movements, as they allow for economically feasible production of next generation optical equipment via significantly less energy intensive fabrication processes.

Appendices

Appendix A: MATLAB Script for Determining Film Thicknesses from AFM Data

The subsequent MATLAB script was used to determine PMMA and titania film thickness from 2D height profiles extracted from experimental AFM data. A linear regression of the glass substrate data points is taken and generates the best linear equation of fit. This cutoff is input manually by the user by changing the "cutoff" variable. Then all x-values are plugged into this equation, and this generates a new set of z (height) values. Finally, the original z-values are subtracted from the corrected z-values to generate a plot that is no longer influenced by the glass substrate's innate slant. This is shown in Figure 10. The script finds the x-indices corresponding to the largest difference between two consecutive z-values, indexes both forward and backward any number of indices depending on the sample, and subtracts new corresponding z-values to determine the layer thickness. The number of index iterations is determined by the user's definition of the variable "slopeThresh." The script is provided in Figure A.1:

```
%%% Plotting Normalization Code Section

data_in = readmatrix('40d_P10_4_slice3.txt'); %Read File

cutoff = 6;        %linear regression cutoff variable
[val,indx] = min(abs(data_in(:,1)-cutoff));      %Find where X value becomes cutoff
B = [ones(indx,1) data_in(1:indx,1)]\data_in(1:indx,2); %Calculate Linear Regression (intercept, slope)
data_out = [data_in(:,1) (data_in(:,2)-B(1))-B(2).*data_in(:,1)]; %Subtract line appropriatley
plot(data_out(:,1),data_out(:,2)) %plot new data
zVals = data_out(:,2);%isolate heights
xCoords = data_out(:,1); %isolate X coords
%hold on
%plot(data_in(:,1),data_in(:,2)-B(1)) (plot old data with y int set to zero if desired)

%%% Finding max slope and relevant indices
slopeThresh = 20; %set number of points to move forward and back by
slopes = diff(zVals);
slopes = abs(slopes);    %make all slope values positive
maxSlope = max(slopes); %find maximum slope
indexS = find(slopes == maxSlope); %find location of max slope
coordinateMaxS = xCoords(indexS);  %find coordinate location of max slope
indexSL = indexS - slopeThresh; %find index threshhold steps back
coordinateSL = xCoords(indexSL); % find coordinate location of x coord lower bound
indexSU = indexS + slopeThresh; %find index threshold steps forward
coordinateSU = xCoords(indexSU); %find index threshold of x coord upper bound

%%% Calculating Thickness
filmCoord = zVals(indexSU);                    %useful output variable
glassCoord = zVals(indexSL);                   %useful output variables
thickness = zVals(indexSU) - zVals(indexSL);   %find thickness
thickness = abs(thickness);                    %take abs of thickness
```

Figure A.1: MATLAB script for calculating film thicknesses from experimental AFM data.

Appendix B: Validating Experimental Single-Layer Titania Film Reflectance Measurements

Figure 12 demonstrates the degree of noisiness associated with reflectance probe measurements for single-layer titania film measurements. This is attributed to a key equipment limitation: oversaturation of the reflectance probe with the light source needed to provide a reflectance spectra that covered a sufficiently wide range of wavelengths across the visible regime. As such, the integration time during these measurements was set to the minimal 1ms option. To ensure accuracy of the general shape of each film's reflectance spectra at this integration time, several titania films were created with the TTIP1 and TTIP2 precursor solutions. Titania film thicknesses were expected to vary as an inherent property of TTIP1 being less concentrated than TTIP2. To generate more thicknesses, the spincoating deposition RPM was

changed between 2000, 3000, and 4000 RPM for each solution to create six samples. These noisy spectra were then plotted against approximate OpenFilters projections, generated for each by maintaining the constant literature RI value of 2.12 while varying film thickness in increments of 1nm until the best overlap was observed. This was a crude test done to visualize generic curve shapes, and confirm that the expected forms were present despite the noisiness of the spectra. The expected shape variations did emerge, ensuring that the eventual Chi-squared test and polynomial fit done to optimize the effective titania film RI was accurate. The experimental reflectance spectra and approximate OpenFilters are provided here. Note that the large inflation of the experimental tail as compared to the theoretical plots is attributed to use of the constant 2.12 RI, and high degrees of light scattering encountered at larger wavelengths.
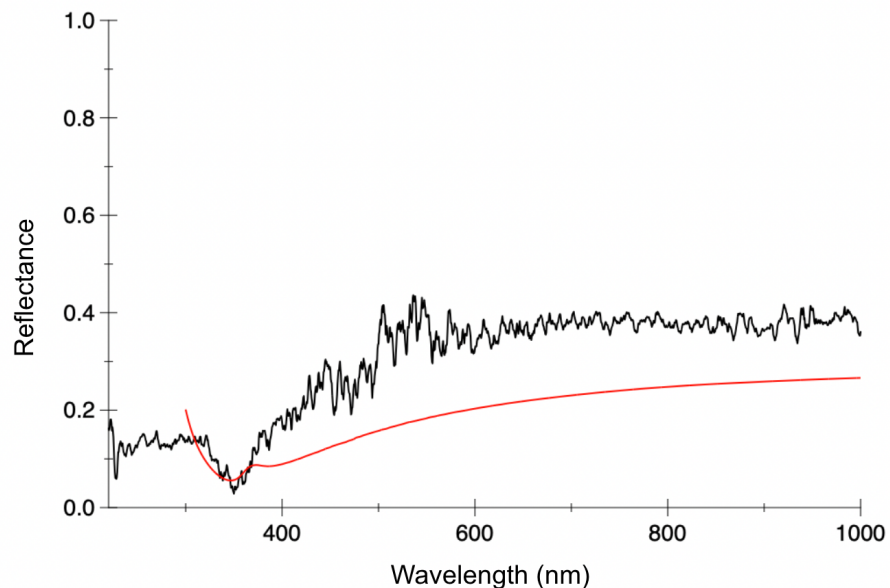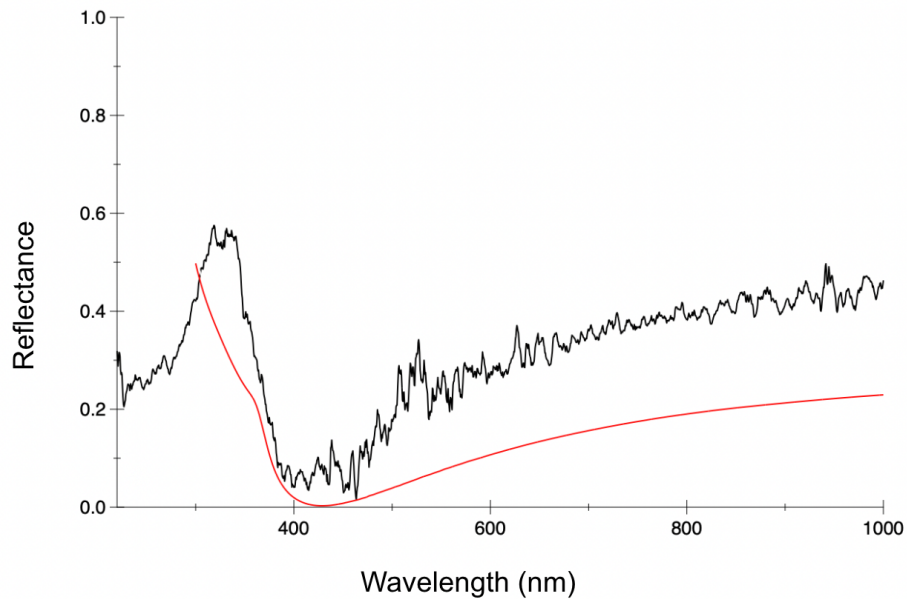

Figure B.1: Experimental reflectance spectra (black) for a TTIP1 film deposited on a glass substrate at 4000 RPM. This is plotted against an OpenFilters-Generated theoretical curve (red) for a 37nm thick titania film with a constant RI of 2.12, which was determined to have the best overlap out of all generated spectra with other thicknesses.
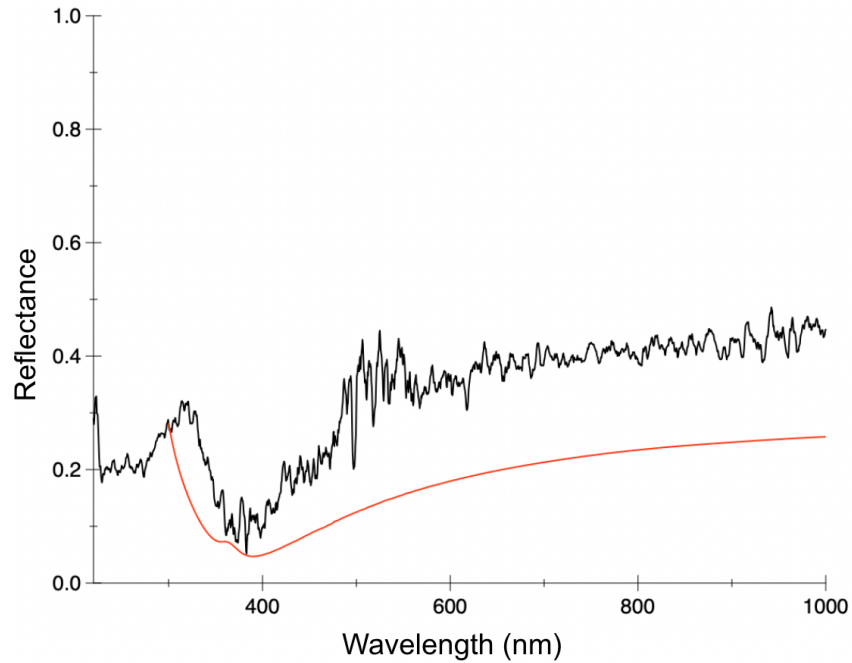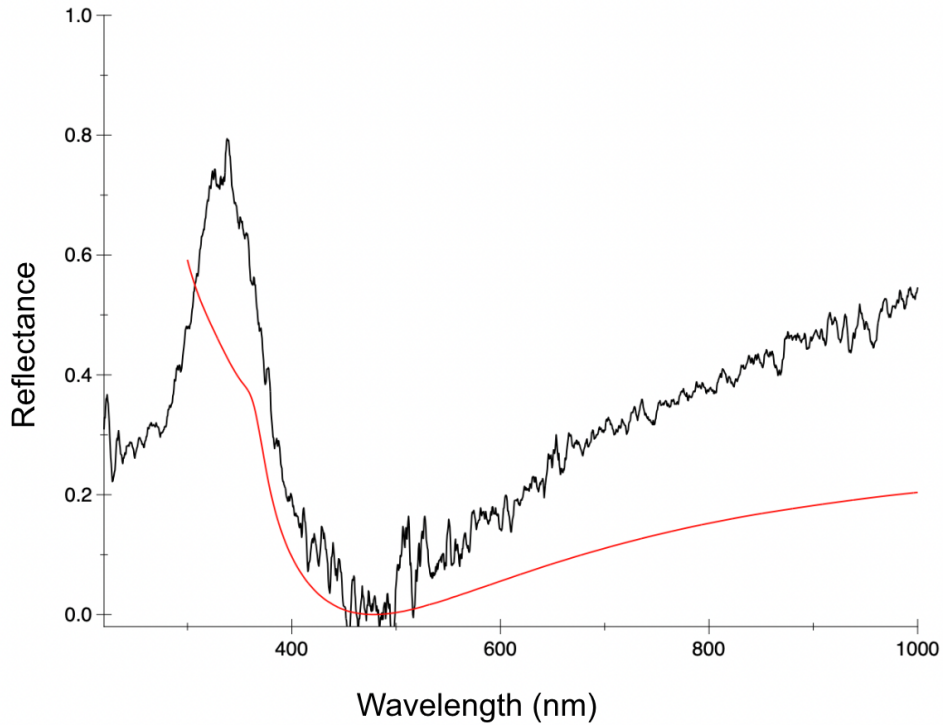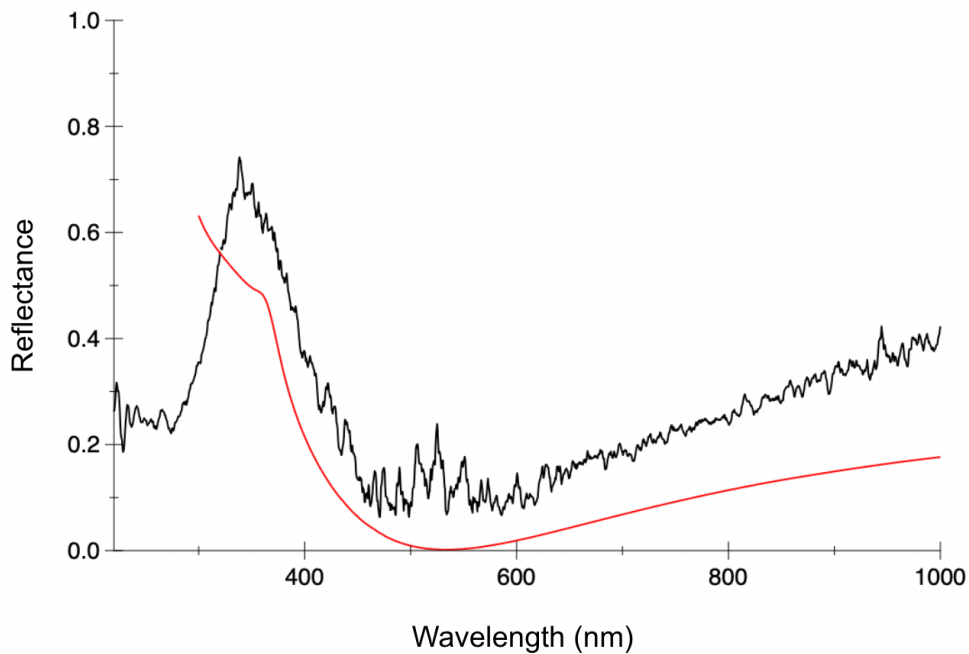
Figure B.2: Experimental reflectance spectra (black) for a TTIP1 film deposited on a glass substrate at 3000 RPM. This is plotted against an OpenFilters-Generated theoretical curve (red) for 40nm thick titania film with a constant RI of 2.12, which was determined to have the best overlap out of all generated spectra with other thicknesses.

Figure B.3: Experimental reflectance spectra (black) for a TTIP1 film deposited on a glass substrate at 2000 RPM. This is plotted against an OpenFilters-Generated theoretical curve (red) for 49nm thick titania film with a constant RI of 2.12, which was determined to have the best overlap out of all generated spectra with other thicknesses.
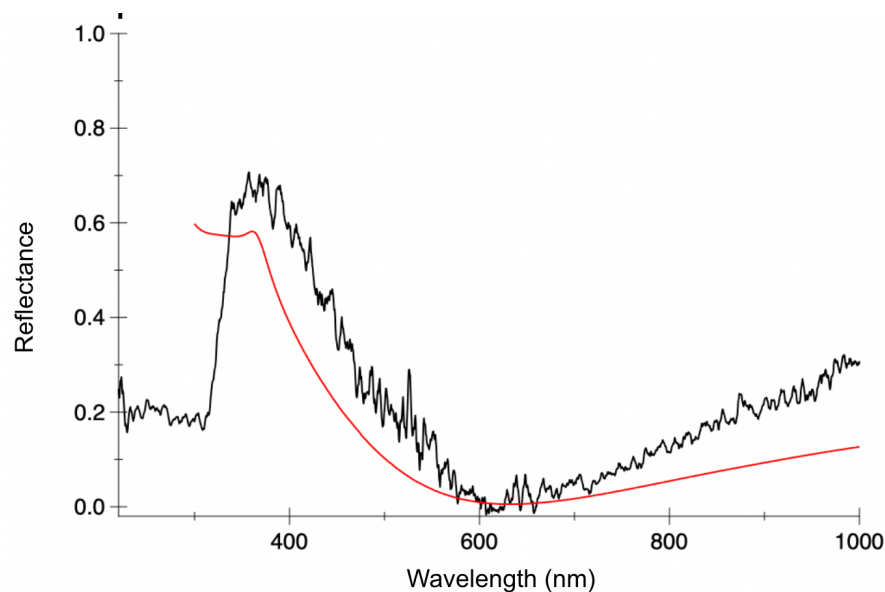
Figure B.4: Experimental reflectance spectra (black) for a TTIP2 film deposited on a glass substrate at 4000 RPM. This is plotted against an OpenFilters-Generated theoretical curve (red) for 56nm thick titania film with a constant RI of 2.12, which was determined to have the best overlap out of all generated spectra with other thicknesses.

Figure B.5: Experimental reflectance spectra (black) for a TTIP2 film deposited on a glass substrate at 3000 RPM. This is plotted against an OpenFilters-Generated theoretical curve (red) for 63nm thick titania film with a constant RI of 2.12, which was determined to have the best overlap out of all generated spectra with other thicknesses.

Figure B.5: Experimental reflectance spectra (black) for a TTIP2 film deposited on a glass substrate at 2000 RPM. This is plotted against an OpenFilters-Generated theoretical curve (red) for 75nm thick titania film with a constant RI of 2.12, which was determined to have the best overlap out of all generated spectra with other thicknesses.

Appendix C: Comparing 15-Layer DBR Stacks to OpenFilters Plots

Due to the unique optical properties of titania sol gel films, an effective refractive index for these layers was determined as a function of wavelength from experimental data. This process for deriving this function is explained in detail in Chapter 2.1.2. Figure 24 provides a comparison of DBR-I's empirical reflectance spectra, an OpenFilters plot using a constant 2.12 literature value as the RI for titania layers, and an OpenFilters plot that uses the optimized effective RI model for these layers instead. It is clear that the optimized model produces theoretical reflectance spectra that better match the experimental data than the constant literature value. These comparisons for the other DBR's that constitute the continuum shown in Figure 26 are provided here:
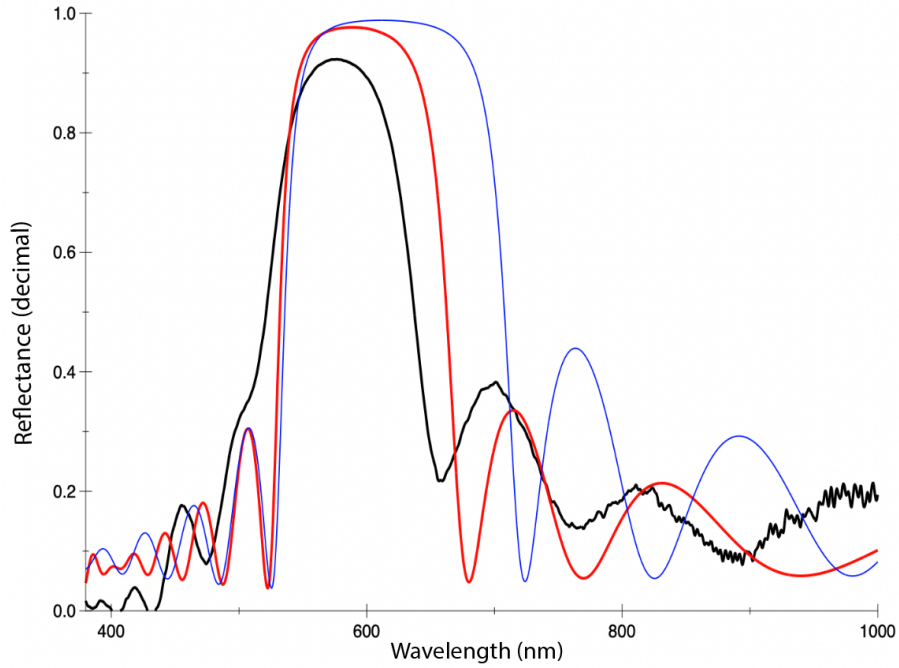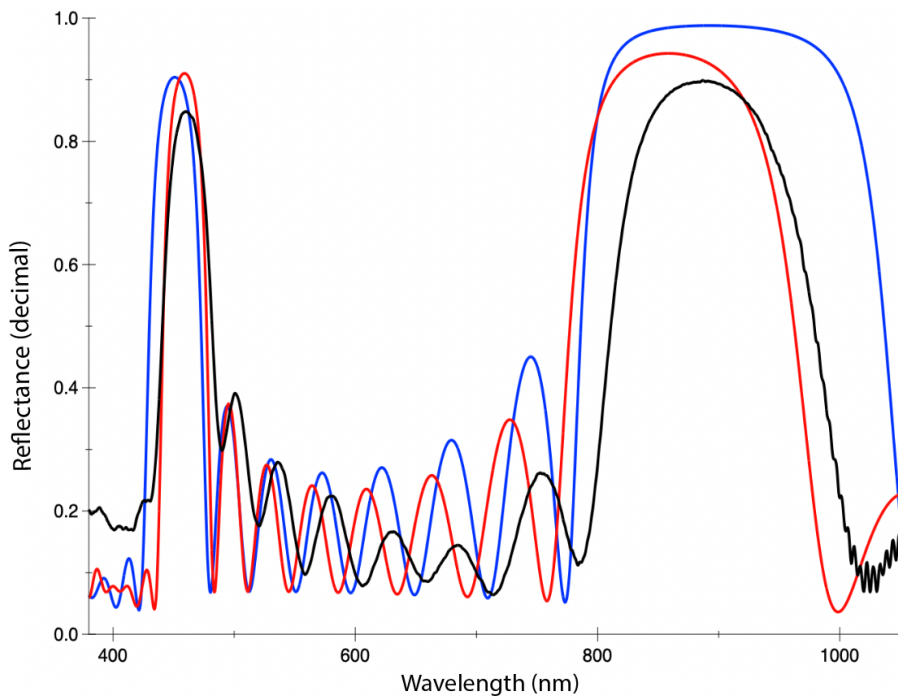
Figure C.1: Comparison of DBR-D's empirical reflectance spectra (black), theoretical reflectance spectra using a literature constant of 2.12 for the effective titania film RI (blue), and the theoretical reflectance spectra using the RI function for the titania films derived in this study (red).
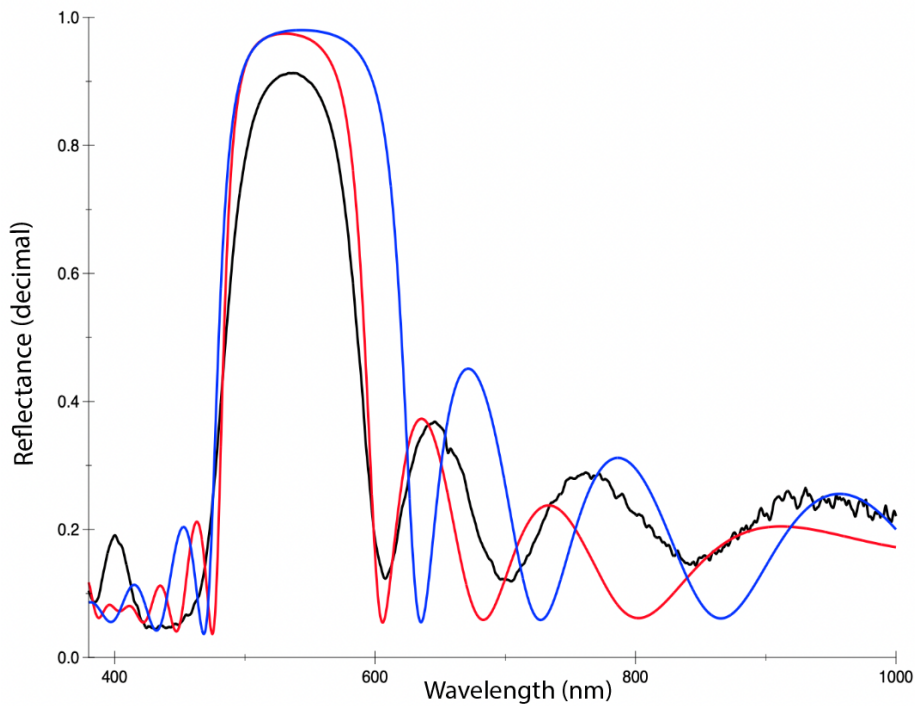
Figure C.2: Comparison of DBR-E's empirical reflectance spectra (black), theoretical reflectance spectra using a literature constant of 2.12 for the effective titania film RI (blue), and the theoretical reflectance spectra using the RI function for the titania films derived in this study (red).
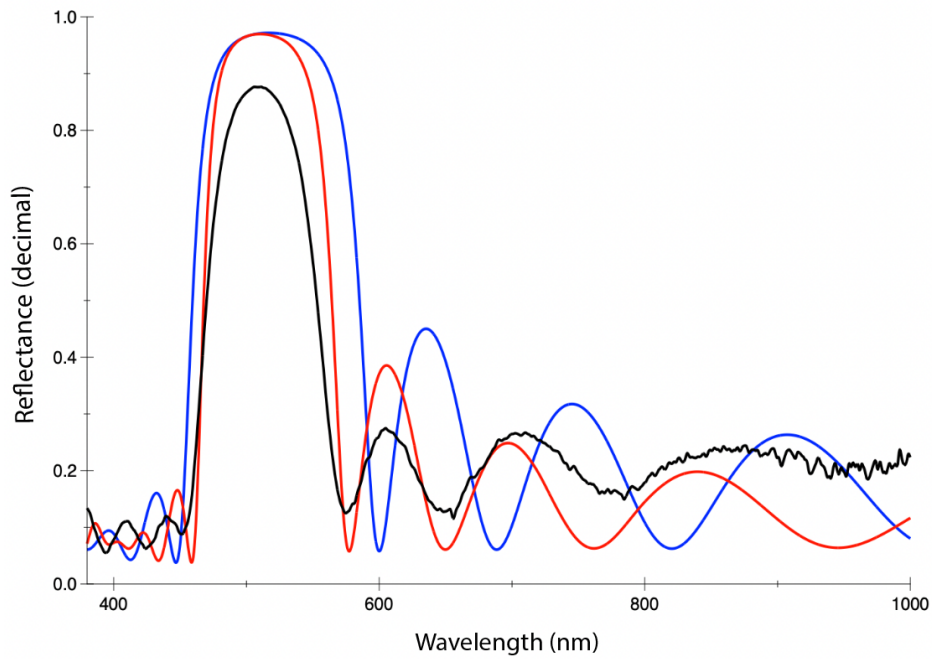
Figure C.3: Comparison of DBR-F's empirical reflectance spectra (black), theoretical reflectance spectra using a literature constant of 2.12 for the effective titania film RI (blue), and the theoretical reflectance spectra using the RI function for the titania films derived in this study (red).

Figure C.4: Comparison of DBR-G's empirical reflectance spectra (black), theoretical reflectance spectra using a literature constant of 2.12 for the effective titania film RI (blue), and the theoretical reflectance spectra using the RI function for the titania films derived in this study (red).
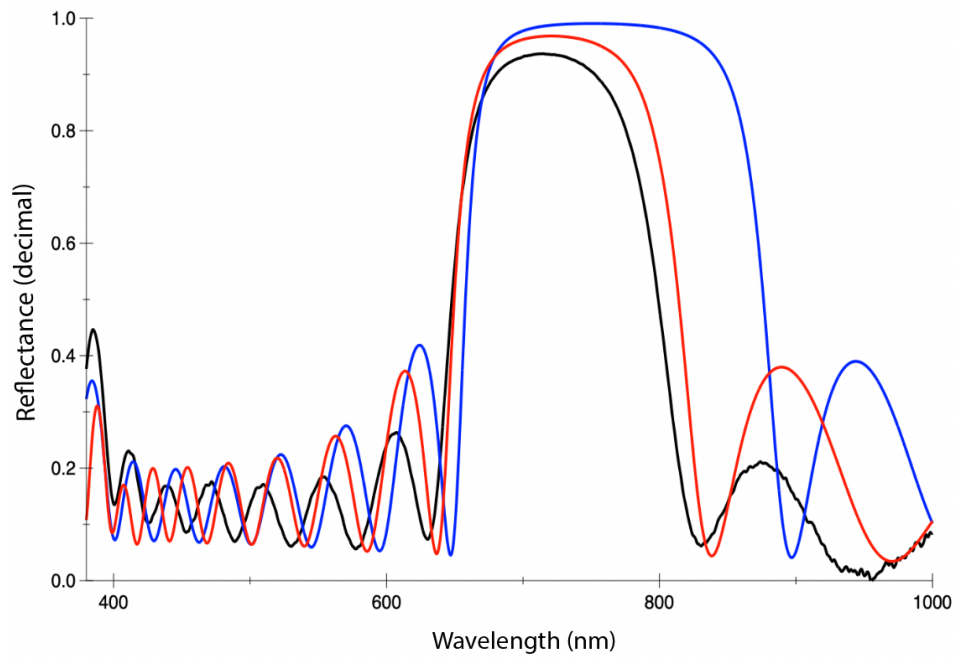
Figure C.5: Comparison of DBR-H's empirical reflectance spectra (black), theoretical reflectance spectra using a literature constant of 2.12 for the effective titania film RI (blue), and the theoretical reflectance spectra using the RI function for the titania films derived in this study (red).

Bibliography

[1]   "Five Ways to Jumpstart the Renewable Energy Transition Now." United Nations. https://www.un.org/en/climatechange/raising-ambition/renewable-energy-transition?gclid=Cj0KCQjwkOqZBhDNARIsAACsbfJu7SIRdu7S_diECM0q0mg16_hG6039cUr8eVTt8lNMEgIEsQ8k1tMaApypEALw_wcB. (accessed October 6, 2022).

[2]   "EIA Predicts Nearly 50% Increase in World Energy Usage by 2050, led by Growth in Asia." U.S. Energy and Information Administration. https://www.eia.gov/todayinenergy/detail.php?id=41433. (accessed October 7, 2022).

[3]   I. Papakonstantinou, M. Portnoi, and M. Debije, "The Hidden Potential of Luminescent Solar Concentrators," Advanced Energy Materials, vol. 11, no. 3, Nov. 2020.

[4]   P. Lova, G. Manfredi, and D. Comoretto, "Advances in Functional Solution Processed Planar 1D Photonic Crystals," *Advanced Optical Materials,* vol. 6, no. 24 Dec. 2018.

[5]   R. Yew, S. Karuturi, H. Tan, and C. Jagadish*,* "Chapter Eight – Nanostructured Photoelectrodes via Template-Assisted Fabrication," *Semiconductors and Semimetals,* vol. 97, pp. 289-313, 2017.

[6]   R. Baets, "Thin Films," in *Photonics,* Ghent, Belgium: Ghent University, 2010, ch. 3, pp. 12-15.

[7]   I. V. Minin, O. V. Minin, and G. V. Shuvalov, "Dielectric Wavelength-Scaled Metalenses Based on an Anomalous Apodization Effect for Photoconductive Optical-to-Terahertz Switches," *2021 XV International Scientific-Technical Conference on Actual Problems Of Electronic Instrument Engineering (APEIE)*, pp. 38-4, Nov. 2021

.

[8]   M. Anaya, A. Rubino, M. Calvo, and H. Míguez, "Solution Processed High Refractive Index Contrast Distributed Bragg Reflectors," *Journal of Materials Chemistry C,* vol. 4, pp. 4532-4537, Mar. 31, 2016.

[9]   W. R. Algar et. al, "Photoluminescent Nanoparticles for Chemical and Biological Analysis and Imaging," Chemical Reviews, vol. 121, no. 15, pp. 9243-9358, Jul, 2021.

[10]   P. Kambhampati, "Nanoparticles, Nanocrystals, and Quantum Dots: What are the Implications of S*ize in Colloidal Nanoscale Materials?"* The Journal of Physical Chemistry Letters, vol. 12, no. 20, pp. 4769-4779, May 2021.

[11]   A. Polman and H. Atwater, "Photonic Design Principles for Ultrahigh-efficiency Photovoltaics," *Nature Materials*, vol 11, pp. 174-177, Mar. 2012.

[12]   A. Brown, *et al.*, "Precise Control of $CsPbBr_3$ Perovskite Nanocrystal Growth at Room

Temperature: Size Tunability and Synthetic Insights," *Chemistry of Materials*, vol. 33, no. 7, pp. 2387-2397, Mar. 2021.

[13] B. Zhang *et al*.," Stable and Size Tunable $CsPbBr_3$ Nanocrystals Synthesized with Oleylphosphonic Acid," *Nano Letters*, vol. 20, no. 21, pp.8847-8854, Nov. 2020.

[14] N. Bronstein, "Material and Optical Design Rules for High Performance Photoluminescent Solar Concentrators" PhD Thesis, Dept. of Chemistry, University of California, Berkeley, Berkeley, CA, USA, 2015.

[15] C. Eisler *et al.,* "Photoluminescent Concentrator Design for High Efficiency, Low Cost Multijunction Photovoltaics," *Frontiers in Photonics*, Jul. 2022.

[16] "LED Lighting." U.S. Department of Energy. https://www.energy.gov/energysaver/led-lighting#:~:text=The%20high%20efficiency%20and%20directional,modular%20lighting%2C%20and%20task%20lighting. (accessed October 7, 2022).

[17] M. Jurow, *et al*, "Manipulating Transition the Dipole Moment of $CsPbBr_3$ Perovskite Nanocrystals for Superior Optical Properties," *Nano Letters*, vol. 19, no. 4, pp. 2489-2496, Mar. 2019.

[18] G. Pacchioni "Highly Efficient Perovskite LEDs," *Nature Reviews Materials,* vol. 6, no. 108, Jan. 2021

[19] T. Lin, "Analysis of the Transition Dipole Moment Orientation from Nanoparticles," M.S. Thesis, Dept. of Chemical and Biomolecular Engineering, University of California, Los Angeles, Los Angeles, CA, USA, 2021.

[20] "NIF's Guide to How Lasers Work." Lawrence Livermore National Laboratory. https://lasers.llnl.gov/education/how-lasers-work (accessed October 9, 2022).

[21] X. Shi, B. Wang, L. Zhang, Z. Wang, and L. Liao, "Conducting Inorganic-Organic Hybrid Distributed Bragg Reflectors," *Advanced Materials*, vol. 27, no. 42, pp. 6696-6701, Nov. 2015.

[22] K. Singer et al., "Melt-processed All-polymer Distributed Bragg Reflector Laser," *Optics Express*, vol. 16, no. 14, pp. 10358-10363, 2008.

[23] S. Larouche and L. Martinu, "OpenFilters: Open Source Software for the Design, Optimization, and Synthesis of Optical Filters," *Applied Optics,* vol. 47, no. 13, pp. C291-C230, Jan. 2008.

[24] Purdue University. Chapter 3 Lecture 8 Dispersion. [Lecture]. Available:

https://www.physics.purdue.edu/webapps/index.php/course_document/index/phys322/1727/25/15105

[25]   L. Xu, Y. Yao, N. Bronstein, L. Li, A. P. Alivisatos, and R. Nuzzo, "Enhanced Photon Collection in Luminescent Solar Concentrators with Distributed Bragg Reflectors," ACS Photonics, vol. 3, no. 2, pp. 278-285, Jan. 2016.

[26]   L. DeSilva, R.Gadipalli, A. Donato, T.M.W.J. Bandara, "Reflectivity of 88% for four-period hybrid Bragg mirror from spin coating process," *Optik*, vol. 157, no. 157, pp. 360-364, Mar. 2018.

[27]   N. Valappil, M. Luberto, V.M. Menon, I. Zeylikovich, T.K. Gayen, J. Franco, B.B. Das, R.R. Alfano, "Solution processed microcavity structures with embedded quantum dots, Photonics and Nanostructures," Fundamentals and Applications, vol. 5, no. 4, pp. 184-188, Nov. 2007

[28]   A. Mihi, M.Ocaña, and H. Míguez, "Oriented Colloidal-Crystal Thin Films by Spin-Coating Microspheres Dispersed in Volatile Media," Advanced Materials, vol.18, no. 17, pp. 2244-2249, Aug. 2006.

[29]   S. Shinde, S. Park, and J. Shin, "Spin Synthesis of Monolayer SiO2 Thin Films," Journal of Semiconductors, vol. 36, no.4, 2015.

[30]   Y. Jeon, "Solution Processed Flexible Distributed Bragg Reflector and its Application for Flexible Solar Cells," M.S Thesis, Dept. of Chemistry and Nanoscience, EWHA Women's University Graduate School, Seoul, South Korea, 2021.

[31]   J. Gutmann, "Photonic Luminescent Solar Concentrators," PhD Thesis, Department of Microsystems Engineering, University of Freiburg, Freiburg, Germany, 2014.

[32]   A. Othayoth, B.Srinivas, K. Murugan, and K. Muralidharan, "Poly(methyl methacrylate)/Polyphosphate Blends with Tunable Refractive Indices for Optical Applications", *Optical Materials*, vol. 104, Jun. 2020.

[33]   F. Mont, J. K. Kim, M. Schubert, E. Schubert, and R. Siegel, "High-Refractive-Index TiO_2-Nanoparticle-Loaded Encapsulants for Light-Emitting Diodes," *Journal of Applied Physics*, vol. 103, no. 8, Apr. 2008.

[34]   C. Eisler *et al.*, "The Polyhedral Specular Reflector: A Spectrum-splitting Multijunction Design to Achieve Ultrahight (>50%) Solar Module Efficiencies," *IEEE Journal of Photonics,* vol. 9, no. 1, pp. 174-179, Jan. 2019.